Bénard–Marangoni convection: planforms and related theoretical predictions

By J. BRAGARD† AND M. G. VELARDE

Instituto Pluridisciplinar, Universidad Complutense de Madrid, Paseo Juan XXIII No. 1,
E-28040 Madrid, Spain

A derivation is given of the amplitude equations governing pattern formation in surface tension gradient-driven Bénard–Marangoni convection. The amplitude equations are obtained from the continuity, the Navier–Stokes and the Fourier equations in the Boussinesq approximation neglecting surface deformation and buoyancy. The system is a shallow liquid layer heated from below, confined below by a rigid plane and above with a free surface whose surface tension linearly depends on temperature. The amplitude equations of the convective modes are equations of the Ginzburg–Landau type with resonant advective non-variational terms. Generally, and in agreement with experiment, above threshold solutions of the equations correspond to an hexagonal convective structure in which the fluid rises in the centre of the cells. We also analytically study the dynamics of pattern formation leading not only to hexagons but also to squares or rolls depending on the various dimensionless parameters like Prandtl number, and the Marangoni and Biot numbers at the boundaries. We show that a transition from an hexagonal structure to a square pattern is possible. We also determine conditions for alternating, oscillatory transition between hexagons and rolls. Moreover, we also show that as the system of these amplitude equations is non-variational the asymptotic behaviour ($t \to \infty$) may not correspond to a steady convective pattern. Finally, we have determined the Eckhaus band for hexagonal patterns and we show that the non-variational terms in the amplitude equations enlarge this band of allowable modes. The analytical results have been checked by numerical integration of the amplitude equations in a square container. Like in experiments, numerics shows the emergence of different hexagons, squares and rolls according to values given to the parameters of the system.

1. Introduction

A motionless thin fluid layer heated from below and open to the ambient air is unstable if the vertical temperature gradient overcomes a threshold value (Koschmieder 1993). Above threshold, the liquid layer undergoes a transition from the conduction motionless state to a convective state in which the fluid motion generally exhibits a patterned structure with e.g. hexagonal, roll or square cells. The cause of this instability is the heat-induced gradient in the interfacial tension σ. Indeed, surface tension varies with temperature and or concentration of a solute, hence creating surface stresses and flow (Marangoni effect).

Systematic experimental research on patterned convection began with H. Bénard (1900). Bénard discovered the hexagonal convection cells which are now commonly

† Present address: Istituto Nazionale di Ottica, Largo Enrico Fermi 6, 50125 Firenze, Italy.

referred to as Bénard cells (Koschmieder 1993; Velarde & Normand 1980). The circulation of the fluid in the hexagonal cells is generally upwards in the centre (up-hexagons) and downwards along the rim.

Although Bénard became aware of the role of surface tension and surface tension gradients in his experiments, he failed to recognize its key role consequently. It took five decades to unambiguously assess experimentally that indeed the surface tension gradient rather than buoyancy (Rayleigh 1916) was the cause of Bénard cells in thin liquid films (Block 1956; Koschmieder 1993). Pearson (1958) was the first author to provide a theory explaining the effects of the surface tension gradients on Bénard convection. He studied the stability of a liquid layer open to air and uniformly heated from below. According to Pearson's theory for a critical value of the Marangoni number, which is a dimensionless measure of the surface tension variation, the layer displays a short-wave pattern of stationary cellular convection.

Since these pioneering works many publications have been devoted to this surface-tension-gradient-driven instability, in both experimental and theoretical directions. Several reviews exist (Normand, Pomeau & Velarde 1977; Ostrach 1982; Davis 1987) where the authors discuss the role of buoyancy and surface tension gradients in triggering convective instability. More recently a review article by Cross & Hohenberg (1993) was devoted to non-equilibrium pattern formation, with quite a short section dealing with genuine Bénard cells, i.e. Bénard–Marangoni convection (Koschmieder 1993).

To cope with the analytical difficulties of Navier–Stokes and Fourier equations, one has the alternative of numerical integration, albeit in limiting cases (like with fluids having infinite Prandtl number) as done e.g. by Thess & Orszag (1995), or to develop a weakly nonlinear approach around instability thresholds. Perturbative methods were first applied to Bénard–Marangoni convection by Scanlon & Segel (1967) who used very drastic albeit relevant simplifications, i.e. infinite Prandtl number and semi-infinite liquid layer. They predicted an hexagonal convective pattern in favour of rolls above the onset of instability. They also showed that the hexagonal structure may be stable for subcritical values of the Marangoni number. In parallel, experimental investigations increased our knowledge of the problem. For instance, following the earlier work by Koschmieder, Cerisier *et al.* (1987) and Pampaloni *et al.* (1992) studied the relative stability of rolls and hexagons, and concluded that hexagons give way to rolls when the depth of the fluid is increased (increasing the buoyancy versus the surface tension effects). Another result of Lebon and collaborators is the prediction of a transition from hexagons to rolls for high Marangoni numbers (Cloot & Lebon 1984; Bragard & Lebon 1993). This has not yet been observed in experiments. We shall come back to this point later. Their theory also predicts the existence of a range where both hexagons and roll patterns can coexist. Using group theory, Golubitsky, Swift & Knobloch (1984) have shown the importance of the reflection symmetry in the horizontal midplane in the selection of convective planforms. A recent experiment (Schatz *et al.* 1995) has shown hysteretic behaviour occurring in Bénard–Marangoni convection, to be expected in view of the discrepancy existing between energy and linear stability approaches to the problem (Davis 1969; Davis & Homsy 1980; Castillo & Velarde 1982). The hysteresis corresponds to a 3% subcritical range where both a motionless state and convective hexagonal motion can coexist. Schatz *et al.* found a critical Marangoni number of 84 very close to the predicted value of Pearson theory (i.e. $Ma_c = 79.6$). Another recent experiment (Nitschke & Thess 1995) shows a secondary instability from an hexagonal to a square pattern. The experimental set-up differs from that used by Bénard because the gas layer at the upper surface is very

thin and consequently affects in a rather drastic way the thermal boundary condition at the open surface, a point earlier mentioned by Koschmieder (1993).

We have derived the amplitude equation for the modes of convection beyond threshold, taking account of the dependence of the coefficients of these equations on various dimensionless parameters of the system, and in particular more than a single thermal boundary condition, through a varying, appropriate Biot number (to be defined below).

The basic equations are presented in §2. The linearized problem is studied in §3. Amplitude equations for the hexagonal structure are derived in §4 while in §5 the amplitude equations refer to two modes forming an arbitrary angle. In §6 we first recall results about the relative stability of the different possible patterns of hexagons, rolls and squares and then discuss the influence of variations of the coefficients of the amplitude equations with the dimensionless parameters. In §7 we sketch the method used to integrate the amplitude equations and provide a few significant results. In §8 the Eckhaus instability is studied in the framework of our amplitude equations. Finally, §9 is devoted to conclusions and comments on still open questions.

2. Equations and dimensionless parameters

We consider a thin liquid layer of infinite horizontal extent, confined below by a rigid plane and open above to the ambient air, with a surface whose surface tension linearly varies with the temperature. The fluid is heated from below. If the layer is shallow enough or the experiment is done in a reduced gravity facility we may disregard buoyancy. As we shall also disregard the open surface deformation, gravity is then completely neglected. Moreover, the governing equations of the liquid layer (continuity, Navier–Stokes and Fourier equations) are taken in the Boussinesq approximation, hence density and other physical properties of the system are taken constant (kinematic viscosity v, heat diffusivity κ and thermal capacity C_p). This leads to the following set of equations for the mass, momentum and energy:

$$\nabla \cdot \boldsymbol{v} = 0, \tag{2.1}$$

$$\frac{\partial \boldsymbol{v}}{\partial t} + (\boldsymbol{v} \cdot \nabla)\boldsymbol{v} = -\frac{1}{\rho}\nabla p + v\nabla^2\boldsymbol{v}, \tag{2.2}$$

$$\frac{\partial T}{\partial t} + \boldsymbol{v} \cdot \nabla T = \kappa\nabla^2 T. \tag{2.3}$$

The boundary conditions on the velocity and temperature fields at the bottom plate are

$$\boldsymbol{v} = 0, \tag{2.4}$$

$$\partial_z T - Bi^b\, T = \text{constant}, \tag{2.5}$$

while at the upper free surface the corresponding conditions are

$$w = 0, \tag{2.6}$$

$$\partial_x \sigma = \mu\partial_z u, \tag{2.7}$$

$$\partial_y \sigma = \mu\partial_z v, \tag{2.8}$$

$$\partial_z T + Bi^t\, T = \text{constant}, \tag{2.9}$$

where μ is the dynamic viscosity of the fluid. The Biot number Bi parameterizes

the heat transfer at the boundaries. An approximate formula to evaluate Bi^t (the superscript t refers to the top of the liquid layer) is

$$Bi^t \approx \frac{\lambda_{air}}{\lambda} \frac{k}{\tanh kd_{air}}, \tag{2.10}$$

where λ_{air} and λ are the thermal conductivities of the air and liquid, respectively, k is the dimensionless wavenumber and d_{air} is the ratio of the thickness of the air layer to that of the liquid layer (Normand *et al.* 1977). Taking the numerical values corresponding to the recent experiment by Nitschke & Thess (1995), we have $\lambda_{oil} = 0.14\text{W m}^{-1}\text{ K}^{-1}$ $\lambda_{air} = 0.026\text{W m}^{-1}\text{ K}^{-1}$. With the choice of $k = 2$ we get $Bi^t \approx 0.8$ (note that to get the really correct value, we should iterate because $k = k(Bi^t)$). This value is different from the usual value of $Bi^t = 0$ taken into account for theories and also for experiments with a thick upper air layer. Actually, if we take $d_{air} \to \infty$ in (2.10) for silicone oil open to air, we get that $Bi^t \approx 0.38$ (which is the most common situation in experiments). In the two extreme, opposite cases of $Bi = 0$ and $Bi \to \infty$ we have, respectively, the Neumann condition (poor conductor) and the Dirichlet condition (good conductor). The choice $Bi^t \approx 0; Bi^b \to \infty$ (the superscript b refers to the bottom of the liquid layer) is called the Pearson condition as he first studied this case, which strictly speaking does not correspond to the experiments by Bénard (1900) and by Koschmieder (1993). In the following, we treat the problem without any assumption on the values of Biot numbers.

The assumption of an undeformed open surface corresponds to the limit of strong surface tension. The validity of this assumption is a subtle question (Davis 1987; Hadji 1996) but for a vanishing capillary number, except in the long-wave limit $k \to 0$, we can assume with no loss of generality a flat interface (for further discussion on the generally negligible role played by the deformation of the open surface see Davis & Homsy (1980) and Castillo & Velarde (1982)). For a 1 mm deep silicone oil layer, the capillary number takes the value

$$Ca = \frac{\mu\kappa}{\sigma_0 d} = 5.6 \times 10^{-4}. \tag{2.11}$$

In shallow layers, non-negligible deformability may experimentally bring effects of variable depth along the layer. Under such conditions dry spots may appear in the layer and the possibility also exists for coexistence of hexagons, appearing in the shallower parts, with rolls in the deeper ones (VanHook *et al.* 1995; Schatz *et al.* 1995). A similar situation may also occur if the Biot number is non-uniform along the solid support or along the open surface. Neither of these two possibilities is considered here.

Applying twice the curl to the momentum equations and using the continuity equation, we get in dimensionless form the following set of equations:

$$\nabla^4 w = Pr^{-1} \left[\partial_t \nabla^2 w + \nabla_1^2 N(w) - \partial_{xz}^2 N(u) - \partial_{yz}^2 N(v) \right], \tag{2.12}$$

$$\nabla^2 \left(\nabla_1^2 u + \partial_{xz}^2 w \right) = Pr^{-1} \left[\partial_t \left(\nabla_1^2 u + \partial_{xz}^2 w \right) + \partial_{yy}^2 N(u) - \partial_{xy}^2 N(v) \right], \tag{2.13}$$

$$\nabla^2 \left(\nabla_1^2 v + \partial_{yz}^2 w \right) = Pr^{-1} \left[\partial_t \left(\nabla_1^2 v + \partial_{yz}^2 w \right) + \partial_{xx}^2 N(v) - \partial_{xy}^2 N(u) \right], \tag{2.14}$$

with $N(.) = (\boldsymbol{v} \cdot \nabla)(.)$ and $\nabla_1^2 = \partial_{xx}^2 + \partial_{yy}^2$. $Pr = \nu/\kappa$ is the Prandtl number.

3. Linear stability analysis

To linearize the equations (2.1–2.3) we split the variables (like for example the temperature) into a reference profile and an infinitesimal disturbance, called T'. We have

$$T = T_{ref} + T'. \tag{3.1}$$

Then as the horizontal extent is taken infinite we separate the variables, using a Fourier representation in the horizontal plane (x, y). Expecting no confusion in the reader we omit the prime, hence the disturbance becomes (for the temperature):

$$T = T(z) \exp(i\boldsymbol{k} \cdot \boldsymbol{r}) \tag{3.2}$$

where $\boldsymbol{k} = (k_x, k_y)$ is the horizontal wavenumber of modulus k, and $\boldsymbol{r} = (x, y)$. Although long ago Davis (1969) pointed out that an energy method did not provide the same result as a linear stability analysis, in view of what is known both numerically (Vidal & Acrivos 1966) and experimentally, we assume the exchange of stability to simplify the theory. Thus, eliminating the time-dependence and using the Fourier modes in the equations and in the boundary conditions, the linearized eigenvalue problem is

$$\left(D^2 - k^2\right)^2 W(z) = 0, \tag{3.3}$$

$$\left(D^2 - k^2\right) T(z) + W(z) = 0, \tag{3.4}$$

where D denotes a derivative with respect to z. The corresponding boundary conditions are: at $z = 0$

$$W = 0; \quad DW = 0; \quad DT - Bi^b T = 0, \tag{3.5}$$

and at $z = 1$

$$W = 0; \quad D^2 W + k^2 Ma\, T = 0; \quad DT + Bi^t T = 0, \tag{3.6}$$

where

$$Ma = \frac{-(\partial\sigma/\partial T)\Delta T h}{\mu\kappa}$$

is the Marangoni number.

The eigenfunctions W, T and the eigenvalue Ma are, respectively,

$$W(z) = C \left[\{1 + (k \coth k - 1)z\} \sinh kz - kz \cosh kz\right], \tag{3.7}$$

$$T(z) = C\, T(z, Bi^t, Bi^b), \tag{3.8}$$

$$Ma = Ma(k, Bi^t, Bi^b), \tag{3.9}$$

where the constant C is fixed by the normalization

$$\int_0^1 W(z)\,dz = 1. \tag{3.10}$$

For each pair (Bi^t, Bi^b) the minimum of the curve $Ma = Ma(k)$ gives the critical eigenvalue and corresponding wavenumber, respectively (Ma_c, k_c). At threshold, the perturbation of wavenumber k_c starts to grow and the motionless liquid layer becomes unstable as the linear stability analysis gives a sufficient condition for instability (Pearson 1958). Above threshold, linear theory is unable to predict which planform
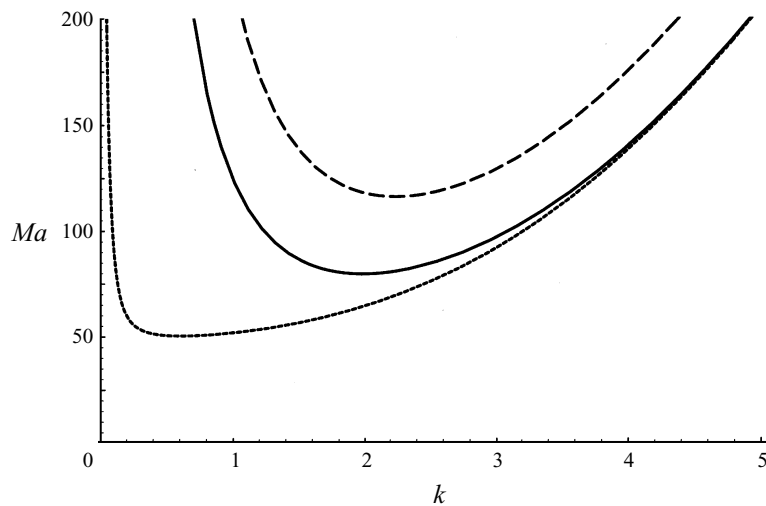
FIGURE 1. Marginal stability curves, Ma vs. k. The solid line refers to the Pearson solution with $Bi^t = 0$ and $Bi^b \to \infty$. The dashed line corresponds to $Bi^t = 1$ and $Bi^b \to \infty$, and the dotted line corresponds to $Bi^t = 0$ and $Bi^b = 0.01$.

will be supercritically selected (hexagons, rolls, squares). Moreover, the planform may also be affected by the heat transfer characteristics at the boundaries, hence by the Biot numbers. Figure 1 gives the marginal stability curves for different values of Bi. For vanishing Bi^b the wavenumber tends to zero, hence the dimension of the cell scales with the lateral extent of the system which is infinity. In this limiting case our nonlinear analysis fails to be applicable, but other theories have dealt with it (see e.g. Knobloch 1990; Shtilman & Sivashinsky 1991; Golovin, Nepomnyashchy & Pismen 1995). In what follows, we shall study the system in the vicinity of finite, non-vanishing k_c, in order to find which structure is preferred when convection sets in.

4. Amplitude equations for the hexagonal structure

Above the linear instability threshold, we look for evolution equations for the amplitude and the phase of the convective state, i.e. for the complex amplitude of the cellular pattern generated by the instability. We use the method of multiple scales in the (x, y, z, t)-space. Then, starting from the basic equations (2.1)–(2.3), we obtain a set of nonlinear partial differential equations that govern the amplitude of the critical modes, hence describing slow modulations in space or time of the convective pattern. The form of the amplitude equations can also be derived using symmetry considerations, and the underlying 'microscopic' equations are needed only to evaluate the coefficients in these amplitude equations. Another possible way to determine the coefficients is to take advantage of knowledge from the experiments.

The method of multiple scales to determine the coefficients consists in separating the time and space variables into fast and slow variables (see e.g. Newell & Whitehead 1969). We introduce a small parameter δ, which is the ratio between the fast and slow spatial variables. Using this, we are able to separate the fast process of instability from the slower evolution of convective structures and the dynamics of defects. As δ becomes an ordering parameter, from the original nonlinear problem we get a hierarchy of linear equations in powers of δ. The left-hand side of each of these

equations is the same linear operator, hence the need of a solvability condition. We require that the right-hand side of each equation in the hierarchy to be orthogonal to the solution of the adjoint linear problem (Fredholm alternative). This condition gives a constraint on the functional dependence of the amplitude, thus leading to the sought amplitude equations.

Linear analysis gives the critical Marangoni number Ma_c for instability and determines the wavenumber k_c of the unstable modes at threshold. However, the direction of $\boldsymbol{k}$ is arbitrary; this degeneracy in orientation comes from the isotropy in the horizontal, infinitely extended plane. There is another degeneracy related to the translation invariance of the layer. These degeneracies do not result from the linear approximation but from symmetries of the chosen geometry, hence persist in the nonlinear analysis. On the other hand, there is a pattern degeneracy that results from the linear approximation. Indeed, any superposition of normal modes (e.g. for temperature)

$$T(\boldsymbol{r}, z) = T(z) \sum_p A_p \exp(\mathrm{i}\boldsymbol{k}^{(p)} \cdot \boldsymbol{r}) \tag{4.1}$$

with $|\boldsymbol{k}^{(p)}| = k_c$ and where the A_p are constant coefficients, is a solution of the linear problem. As T is real, we must impose the conditions $A_{-p} = \overline{A_p}$ and $\boldsymbol{k}^{(-p)} = -\boldsymbol{k}^{(p)}$, but the number of non-zero A_p, i.e. the shape of the pattern, and their modulus, i.e. the amplitude of the temperature perturbation, remain undetermined. To study the hexagonal structure we start the analysis for three wavevectors having 120° angle separation, thus forming a resonant triad. The problem is to determine how the convection amplitude $|A_p|$ saturates above threshold due to nonlinear interactions (Malkus & Veronis 1958; Schlüter, Lortz & Busse 1965; Busse 1978). The solution for the perturbations is (for example for the temperature)

$$T = \delta T_1 + \delta^2 T_2 + \delta^3 T_3 + o(\delta^3). \tag{4.2}$$

The scaling for the slow variables is

$$X = \delta x; \quad Y = \delta y; \quad \tau = \delta^2 t \tag{4.3}$$

and for the fast variables

$$\tilde{x} = x; \quad \tilde{y} = y; \quad \tilde{t} = t. \tag{4.4}$$

Using these scalings the derivatives are

$$\partial_t = \partial_{\tilde{t}} + \delta^2 \partial_\tau, \tag{4.5}$$

$$\nabla_{1x} = \nabla_{1\tilde{x}} + \delta \nabla_{1X} \tag{4.6}$$

with ∇_{1X} and $\nabla_{1\tilde{x}}$ denoting the horizontal gradient for the slow and fast variables, respectively (in the following we omit the tilde in the notation). Note that we have used a different scaling for slow time τ and slow space variables (X, Y). In our case the justification of this comes from the fact that the subcritical region (the region where both the hexagonal pattern and the conductive state may coexist) is small. This allows δ^2 to be taken for the slow time scale rather than δ as done by other authors (Kubstrup, Herrero & Pérez-García 1996). This choice yields that nonlinear saturation and spatial diffusion come together in the amplitude equations. A more rigorous proof of the above scalings demands that we consider simultaneously a slow time scale $\tau_1 = \delta t$ as well as $\tau = \delta^2 t$ and then proceed to an adiabatic elimination over the small subcritical region. We shall not dwell on this delicate matter but use the above defined scalings as a pragmatic procedure. The eigenvalue is expanded also

using the smallness parameter δ

$$Ma = Ma_c + \delta Ma^{(1)} + \delta^2 Ma^{(2)}. \tag{4.7}$$

We insert all the above expressions in the basic equations and get successive equations at each power in δ. At the first order in δ we recover the linear problem, as expected. The function in the (x, y)-plane (which as earlier stated is not determined by the linear analysis) is now chosen to satisfy the hexagonal symmetry. Three modes with wave vector of modulus k_c are chosen in the wave-space oriented at $120°$, $\boldsymbol{k}^{(1)} + \boldsymbol{k}^{(2)} + \boldsymbol{k}^{(3)} = \boldsymbol{0}$. This choice fits well with the experimental evidence offered by Bénard (1900) and by Koschmieder (1993). However, note that the combination of a triad of modes not only leads to the hexagonal structure. It also permits a roll structure. By introducing only three horizontal modes, we certainly simplify the intricate dynamics of mode selection in the convective state. We shall address this question later on by adding other critical modes in the planform function.

The solution at first order is

$$\left.\begin{aligned}
w_1 &= W(z) \left[A_1(X, Y, \tau) \exp(i\boldsymbol{k}^{(1)} \cdot \boldsymbol{r}) + A_2 \exp(i\boldsymbol{k}^{(2)} \cdot \boldsymbol{r}) + A_3 \exp(i\boldsymbol{k}^{(3)} \cdot \boldsymbol{r}) + \text{c.c.} \right], \\
T_1 &= T(z) \left[A_1 \exp(i\boldsymbol{k}^{(1)} \cdot \boldsymbol{r}) + A_2 \exp(i\boldsymbol{k}^{(2)} \cdot \boldsymbol{r}) + A_3 \exp(i\boldsymbol{k}^{(3)} \cdot \boldsymbol{r}) + \text{c.c.} \right], \\
\boldsymbol{u}_1^H &= \frac{\mathrm{D}W}{k^2} \nabla_{1x} \left[A_1 \exp(i\boldsymbol{k}^{(1)} \cdot \boldsymbol{r}) + A_2 \exp(i\boldsymbol{k}^{(2)} \cdot \boldsymbol{r}) + A_3 \exp(i\boldsymbol{k}^{(3)} \cdot \boldsymbol{r}) + \text{c.c.} \right],
\end{aligned}\right\} \tag{4.8}$$

where the subscript number corresponds to the order of the solution and the superscript H denotes horizontal components of the velocity (u, v).

The next order is δ^2. We have

$$\left(\nabla_{1x}^2 + \partial_{z^2} \right) T_2 + w_2 = \left(\boldsymbol{u}_1^H \cdot \nabla_{1x} \right) T_1 + w_1 \partial_z T_1 - 2 \left(\nabla_{1x} \cdot \nabla_{1X} \right) T_1, \tag{4.9a}$$

$$\left(\nabla_{1x}^2 + \partial_{z^2} \right)^2 w_2 = Pr^{-1} \left[\nabla_{1x}^2 \left\{ \left(\boldsymbol{u}_1^H \cdot \nabla_{1x} \right) w_1 + w_1 \partial_z w_1 \right\} \right. \\
\left. - \partial_z \nabla_{1x} \cdot \left\{ \left(\boldsymbol{u}_1^H \cdot \nabla_{1x} \right) \boldsymbol{u}_1^H + w_1 \partial_z \boldsymbol{u}_1^H \right\} \right] - 4 \left(\nabla_{1x}^2 + \partial_{zz} \right) \left(\nabla_{1x} \cdot \nabla_{1X} \right) w_1, \tag{4.9b}$$

$$\left(\nabla_{1x}^2 + \partial_{z^2} \right) \left(\nabla_{1x}^2 u_2 + \partial_{zx} w_2 \right) = Pr^{-1} \left[\partial_{yy}^2 \left\{ \left(\boldsymbol{u}_1^H \cdot \nabla_{1x} \right) u_1 + w_1 \partial_z u_1 \right\} \right. \\
\left. - \partial_{yx}^2 \left\{ \left(\boldsymbol{u}_1^H \cdot \nabla_{1x} \right) v_1 + w_1 \partial_z v_1 \right\} \right] - 4 \nabla_{1x}^2 \left(\nabla_{1x} \cdot \nabla_{1X} \right) u_1 \\
- 2 \partial_{zz} \left(\nabla_{1x} \cdot \nabla_{1X} \right) u_1 - 2 \partial_{zx} \left(\nabla_{1x} \cdot \nabla_{1X} \right) w_1 - \partial_{zX} \left(\nabla_{1x}^2 + \partial_{zz} \right) w_1. \tag{4.9c}$$

The boundary conditions are unchanged except for that containing the Marangoni number which now reads

$$\partial_{zz} w_2 - Ma_c \nabla_{1x}^2 T_2 = Ma^{(1)} \nabla_{1x}^2 T_1 + 2 Ma_c \left(\nabla_{1x} \cdot \nabla_{1X} \right) T_1. \tag{4.10}$$

To solve equations (4.9), (4.10), we compute the right-hand side by introducing the first-order solution; then we collect the terms in the right-hand side which have the same wavenumber modulus. In this case the moduli found are the first harmonic combination of the resonant triad, say $(0, 1, \sqrt{3}, 2) * k$ modes. If we separate variables, we get a set of ordinary differential equations for each mode. The solution of these equations is given in Appendix B.

The solvability condition is

$$\langle \boldsymbol{u}^+, N(\boldsymbol{u}) \rangle = 0, \tag{4.11}$$

where the symbol $\langle .. \rangle$ denotes the scalar product defined in Appendix A. Applying the solvability condition to the set of equations corresponding to the k-mode, with separation of variables we obtain

$$A_2^* A_3^* \left[\int_0^1 T^+ \left\{ 2W\mathrm{D}T + T\mathrm{D}W \right\} \mathrm{d}z \right.$$

$$\left. + Pr^{-1} \int_0^1 W^+ \left\{ 2\mathrm{D}W\mathrm{D}^2W + W\mathrm{D}^3W - 3k^2W\mathrm{D}W \right\} \mathrm{d}z \right]$$

$$- 2\mathrm{i} \left(\boldsymbol{k}^{(1)} \cdot \nabla_{1X} \right) A_1 \left[\int_0^1 T^+ T \mathrm{d}z + 2 \int_0^1 W^+ (\mathrm{D}^2W - k^2W) \mathrm{d}z \right]$$

$$+ (\mathrm{D}W^+ T)|_{z=1} \left[2\mathrm{i}Ma_c \left(\boldsymbol{k}^{(1)} \cdot \nabla_{1X} \right) A_1 - Ma^{(1)}k^2 A_1 \right] = 0. \qquad (4.12)$$

In the particular case of $Bi^t = 0$, $Bi^b \to \infty$ (Pearson 1958), (4.12) reduces to

$$\left[\frac{-44.4}{Pr} + 195.4 \right] A_2^* A_3^* + 6.62 Ma^{(1)} A_1 = 0. \qquad (4.13)$$

We have three such relations, one for each amplitude, obtained by circular permutation of the indices. These relations among the amplitudes are used to integrate the second-order equations (4.9), (4.10). Note that with non-zero $Ma^{(1)}$, we have hexagons while rolls are allowed when $Ma^{(1)}$ vanishes. The next step is to write the third-order equations (4.14), (4.15). We need not solve them but only write the solvability condition in order to get the amplitude equation. We have

$$\left(\nabla_{1x}^2 + \partial_{z^2} \right) T_3 + w_3 = \partial_\tau T_1 + \left(\boldsymbol{u}_1^H \cdot \nabla_{1x} \right) T_2 + \left(\boldsymbol{u}_2^H \cdot \nabla_{1x} \right) T_1 + \left(\boldsymbol{u}_1^H \cdot \nabla_{1X} \right) T_1$$
$$+ w_1 \partial_z T_2 + w_2 \partial_z T_1 - 2 \left(\nabla_{1x} \cdot \nabla_{1X} \right) T_2 - \nabla_{1X}^2 T_1, \qquad (4.14a)$$

$$\left(\nabla_{1x}^2 + \partial_{z^2} \right)^2 w_3 = Pr^{-1} \left[\partial_\tau \left(\nabla_{1x}^2 + \partial_{z^2} \right) w_1 + 2 \left(\nabla_{1x} \cdot \nabla_{1X} \right) \left\{ \left(\boldsymbol{u}_1^H \cdot \nabla_{1x} \right) w_1 + w_1 \partial_z w_1 \right\} \right.$$
$$+ \nabla_{1x}^2 \left\{ \left(\boldsymbol{u}_1^H \cdot \nabla_{1X} \right) w_1 + \left(\boldsymbol{u}_1^H \cdot \nabla_{1x} \right) w_2 + \left(\boldsymbol{u}_2^H \cdot \nabla_{1x} \right) w_1 + w_1 \partial_z w_2 + w_2 \partial_z w_1 \right\}$$
$$- \partial_z \nabla_{1x} \cdot \left\{ \left(\boldsymbol{u}_1^H \cdot \nabla_{1X} \right) \boldsymbol{u}_1^H + \left(\boldsymbol{u}_1^H \cdot \nabla_{1x} \right) \boldsymbol{u}_2^H + \left(\boldsymbol{u}_2^H \cdot \nabla_{1x} \right) \boldsymbol{u}_1^H + w_1 \partial_z \boldsymbol{u}_2^H + w_2 \partial_z \boldsymbol{u}_1^H \right\}$$
$$\left. - \partial_z \nabla_{1X} \cdot \left\{ \left(\boldsymbol{u}_1^H \cdot \nabla_{1x} \right) \boldsymbol{u}_1^H + w_1 \partial_z \boldsymbol{u}_1^H \right\} \right]$$
$$- 4 \left(\nabla_{1x}^2 + \partial_{zz} \right) \left(\nabla_{1x} \cdot \nabla_{1X} \right) w_2 - \left[4 \left(\nabla_{1x} \cdot \nabla_{1X} \right)^2 + 2 \left(\nabla_{1x}^2 + \partial_{zz} \right) \nabla_{1X}^2 \right] w_1. \qquad (4.14b)$$

Again the boundary conditions are unchanged except that containing the Marangoni number which now reads

$$\partial_{zz} w_3 - Ma_c \nabla_{1x}^2 T_3 = Ma^{(1)} \nabla_{1x}^2 T_2 + Ma^{(2)} \nabla_{1x}^2 T_1 + Ma_c \nabla_{1X}^2 T_1$$
$$+ 2Ma_c \left(\nabla_{1x} \cdot \nabla_{1X} \right) T_2 + 2Ma^{(1)} \left(\nabla_{1x} \cdot \nabla_{1X} \right) T_1. \qquad (4.15)$$

Applying once more the solvability condition, we get the amplitude equations at third order. The last step is to eliminate $Ma^{(1)}$ and $Ma^{(2)}$ from the amplitude equations at this order. To do this, we take the problem at order δ^3 hence combining the solvability conditions at orders δ^2 and δ^3 (for further details on a similar problem see Busse 1967). Then returning to the original fast variables $\delta A_j(X, Y, \tau) \to A_j'(x, y, t)$. We use (4.7) where Ma is, say, the experimenter's value, and $\varepsilon = (Ma - Ma_c)/Ma_c$ denotes the departure from the linear threshold and then substitute all these expressions in the solvability condition at order δ^3. Making all these substitutions for the fast variables which are of order unity, we get the following final form of the amplitude equation

(expecting no confusion for the reader, in what follows, we omit the prime):

$$\alpha_t \partial_t A_1 = \alpha_l \varepsilon A_1 + \alpha_d \left(\boldsymbol{k}^{(1)} \cdot \nabla_{1x}\right)^2 A_1 + \alpha_q A_2^* A_3^*$$
$$-g_d |A_1|^2 A_1 - g_{nd} \left(|A_2|^2 + |A_3|^2\right) A_1$$
$$+\mathrm{i}\beta_1 \left[A_3^* \left(\boldsymbol{k}^{(2)} \cdot \nabla_{1x}\right) A_2^* + A_2^* \left(\boldsymbol{k}^{(3)} \cdot \nabla_{1x}\right) A_3^*\right]$$
$$+\mathrm{i}\beta_2 \left[A_2^* \left(\boldsymbol{k}^{(2)} \cdot \nabla_{1x}\right) A_3^* + A_3^* \left(\boldsymbol{k}^{(3)} \cdot \nabla_{1x}\right) A_2^*\right], \qquad (4.16)$$

where

$$\alpha_l = 263.68, \quad \alpha_t = 43.96 + 11.21\ Pr^{-1}, \quad \alpha_q = 97.72 - 22.2\ Pr^{-1},$$
$$g_d = 425.1 + 132.6\ Pr^{-1} + 20.82\ Pr^{-2}, \quad g_{nd} = 579.8 + 289.3\ Pr^{-1} + 3.48\ Pr^{-2},$$
$$\alpha_d = 18.56, \quad \beta_1 = -30.65 - 7.96\ Pr^{-1},$$
$$\beta_2 = -124.2 - 0.51\ Pr^{-1}, \quad \varepsilon = (Ma - Ma_c)/Ma_c.$$

Similar equations exist for A_2 and A_3 (with circular permutation of the indices). Note that the hexagonal solution to (4.16) has A of order α_q/g_d which is fairly small. Therefore the above approach, combining the solvability at order two and three, is valid. The amplitude equations describe the pattern dynamics of the hexagonal structure for weakly supercritical instability ($\delta \ll 1$). The numerical values of the coefficients correspond to a very poor conducting open, upper surface, $Bi^t = 0$ and good conducting rigid, lower plate, $Bi^b \rightarrow \infty$ (Pearson problem). For example g_d and g_{nd} in (4.16) refer to self-saturation and interacting cubic saturation terms of the convective modes. Physically, it means that these terms saturate the linear instability in order to reach a final steady convective regime even near threshold.

A significant result is that the equation (4.16) is a generalized Ginzburg–Landau equation with advective terms ($\beta_i \neq 0$). For such equations there is no Lyapunov functional hence for some values of β we may never reach steady convection. If β vanishes and then we have a variational problem, the Lyapunov functional allows (4.16) to be written in the form

$$\alpha_t \partial_t A_j = -\frac{\delta \mathscr{L}}{\delta A_j^*} \qquad (4.17)$$

with

$$\mathscr{L} = \int \int \mathrm{d}x\,\mathrm{d}y \sum_{j=1}^{3} \left[-\alpha_l \varepsilon |A_j|^2 + \alpha_d \left|\left(\boldsymbol{k}^{(j)} \cdot \nabla_{1x}\right) A_j\right|^2 + \frac{g_d}{2}|A_j|^4\right]$$
$$+g_{nd} \left[|A_1|^2|A_2|^2 + |A_1|^2|A_3|^2 + |A_2|^2|A_3|^2\right] - \alpha_q \left[A_1 A_2 A_3 + \text{c.c.}\right]. \qquad (4.18)$$

The presence of non-variational terms was predicted by Brand (1989) for buoyancy-driven Rayleigh–Bénard convection. The form given above incorporates translation and space reflection symmetries (in the horizontal plane) but the rotation symmetry (for an arbitrary angle) has been broken with the choice (4.1). However, as already shown by Gunaratne (1993) to preserve the rotational symmetry (important if we want to deal with structures of different orientations and fronts) we have to write (4.16) in the following form:

$$\alpha_t \partial_t A_1 = \alpha_l \varepsilon A_1 + \alpha_d \left(\boldsymbol{k}^{(1)} \cdot \nabla_{1x} - \tfrac{1}{2}\mathrm{i}\nabla_{1x}^2\right)^2 A_1 + \alpha_q A_2^* A_3^*$$
$$-g_d |A_1|^2 A_1 - g_{nd} \left(|A_2|^2 + |A_3|^2\right) A_1$$
$$+\mathrm{i}\beta_1 \left[A_3^* \left(\boldsymbol{k}^{(2)} \cdot \nabla_{1x} - \tfrac{1}{2}\mathrm{i}\nabla_{1x}^2\right) A_2^* + A_2^* \left(\boldsymbol{k}^{(3)} \cdot \nabla_{1x} - \tfrac{1}{2}\mathrm{i}\nabla_{1x}^2\right) A_3^*\right]$$
$$+\mathrm{i}\beta_2 \left[A_2^* \left(\boldsymbol{k}^{(2)} \cdot \nabla_{1x}\right) A_3^* + A_3^* \left(\boldsymbol{k}^{(3)} \cdot \nabla_{1x}\right) A_2^* - \mathrm{i}\nabla_{1x}A_2^* \cdot \nabla_{1x}A_3^*\right]. \qquad (4.19)$$

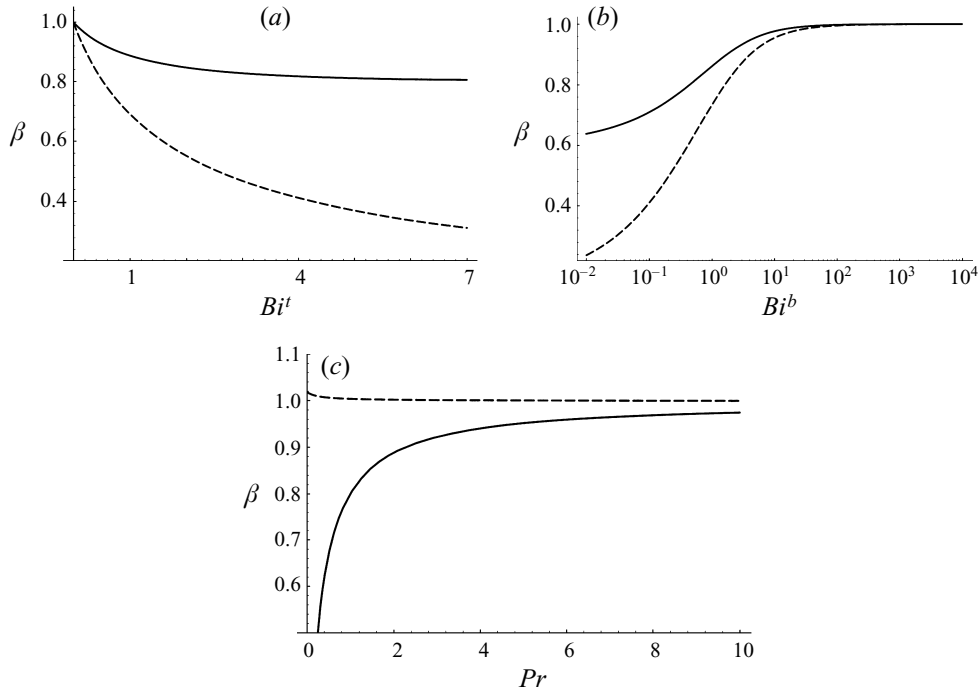FIGURE 2. Variation of β with (a) Bi^t, $Bi^b \to \infty$ and $Pr \to \infty$; (b) Bi^b, $Bi^t = 0$ and $Pr \to \infty$; (c) $Bi^t = 0$ and $Bi^b \to \infty$. The solid lines refer to β_2, the dashed lines to β_1.

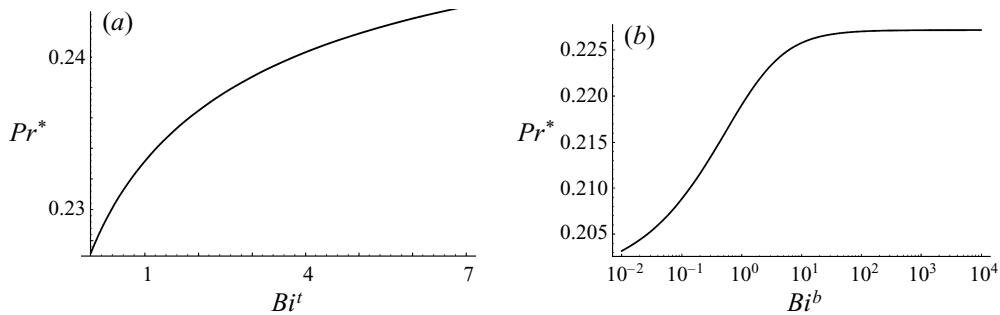FIGURE 3. (a) Variation of Pr^* with Bi^t, $Bi^b \to \infty$ and $Pr \to \infty$, and (b) Bi^b, $Bi^t = 0$; $Pr \to \infty$.

However, for all practical purposes in Bénard convection, the extra higher derivative terms in (4.19) relative to (4.16) are negligible (except when the projection of one of the wavenumbers onto the coordinate axis tends to zero).

For completeness we give the numerical values of the β coefficients of the amplitude equations when the parameters Bi and Pr take different values (figure 2). We first divide all coefficients by α_t to have always unity in front of the time derivative. All plots refer to variations relative to the Pearson case: $Bi^t = 0$, $Bi^b \to \infty$ and $Pr \to \infty$. Figures 3(a) and 3(b) correspond to the values of Pr^* for which the coefficient α_q changes sign. It corresponds to a transition from up-hexagons to down-hexagons (fluid sinking in the centre of the cells) for low values of Pr. In the experiments performed with silicone oils Pr is much higher than Pr^* and only up-hexagons are observed. Pr^* is practically independent of the values of Bi, hence the transition from up- to

down-hexagons is intrinsic to the fluid bulk properties (Prandtl number) and nearly independent of the Biot numbers. Recently, Thess & Bestehorn (1995) have discussed this transition from up- to down-hexagons. They concluded that the transition passes through an intermediate state where rolls are stable and for very low values of *Pr* (e.g. in liquid metals or helium) the pattern evolution offers a seemingly turbulent behaviour. Assenheimer & Steinberg (1996) have described a method for varying the Prandtl number in a buoyancy-driven Rayleigh–Bénard convection experiment. Without changing the working fluid, it suffices to approach the critical point of the liquid (in their experiments they used SF_6). These authors observed domains of down-hexagons coexisting with domains of up-hexagons. In §6, we come back to this question and show how the pattern selection is sensitive to both bulk and boundary properties.

5. Planforms with two modes forming an arbitrary angle

The derivation of the amplitude equations for two modes A_1 and A_2 forming an arbitrary angle θ follows the same procedure as for hexagons. However, with two modes there is no 'resonant' interaction between them and, moreover, the second-order solution depends on the angle θ between the two wavevectors $\boldsymbol{k}^{(1)}$ and $\boldsymbol{k}^{(2)}$. Thus the solution of (3.3), (3.4) for the two modes at first order (in δ) is

$$\left.\begin{aligned}
w_1 &= W(z)\left[A_1(X,Y,\tau)\exp(i\boldsymbol{k}^{(1)}\cdot\boldsymbol{r}) + A_2\exp(i\boldsymbol{k}^{(2)}\cdot\boldsymbol{r}) + \text{c.c.}\right], \\
T_1 &= T(z)\left[A_1\exp(i\boldsymbol{k}^{(1)}\cdot\boldsymbol{r}) + A_2\exp(i\boldsymbol{k}^{(2)}\cdot\boldsymbol{r}) + \text{c.c.}\right], \\
\boldsymbol{u}_1^H &= \frac{DW}{k^2}\nabla_{1x}\left[A_1\exp(i\boldsymbol{k}^{(1)}\cdot\boldsymbol{r}) + A_2\exp(i\boldsymbol{k}^{(2)}\cdot\boldsymbol{r}) + \text{c.c.}\right]
\end{aligned}\right\} \quad (5.1)$$

with $\boldsymbol{k}^{(1)}\cdot\boldsymbol{k}^{(2)} = k^2\cos\theta = k^2\beta$. The next step is to solve the equations at order δ^2 (4.9), (4.10). Introducing the first-order solution in the right-hand side and separating vertical and horizontal variables, we get a set of differential equations with wavevectors of different moduli (Appendix C).

The solvability condition gives

$$Ma^{(1)} = 0, \quad (5.2)$$

hence with two modes there is no subcritical instability and the same occurs for the case of only one mode (rolls). The next step is to introduce the complete second-order solution (which in this case depends on the angle θ) into the third-order equations (4.14), (4.15) and then use the Fredholm alternative. It is not necessary to compute all the terms but it suffices to use the terms already computed from the amplitude equations for hexagons, and only compute the new term, i.e. the off-diagonal cubic term $g(\theta)$. For the two-mode equations, the quadratic terms $A_2^*A_3^*$ and the advective terms (with coefficients β_1 and β_2) do not appear. The coefficient $g(\theta)$ is now angle-dependent, hence we compute it for several values of θ (see figure 4*a*).

Applying the solvability condition, and returning to the fast variables the amplitude equation becomes

$$\alpha_t\partial_t A_1 = \alpha_l\varepsilon A_1 + \alpha_d\left(\boldsymbol{k}^{(1)}\cdot\nabla_{1x}\right)^2 A_1 - g_d|A_1|^2 A_1 - g(\theta)\left(|A_2|^2\right)A_1 \quad (5.3)$$

and a similar equation for A_2 (interchanging the indices 1 and 2). The numerical values of the coefficients are the same as for the hexagons except for $g(\theta)$, the cubic interaction term. This term has to be computed for each value of the angle θ (as the second-order solution depends on θ). We have computed this coefficient for several
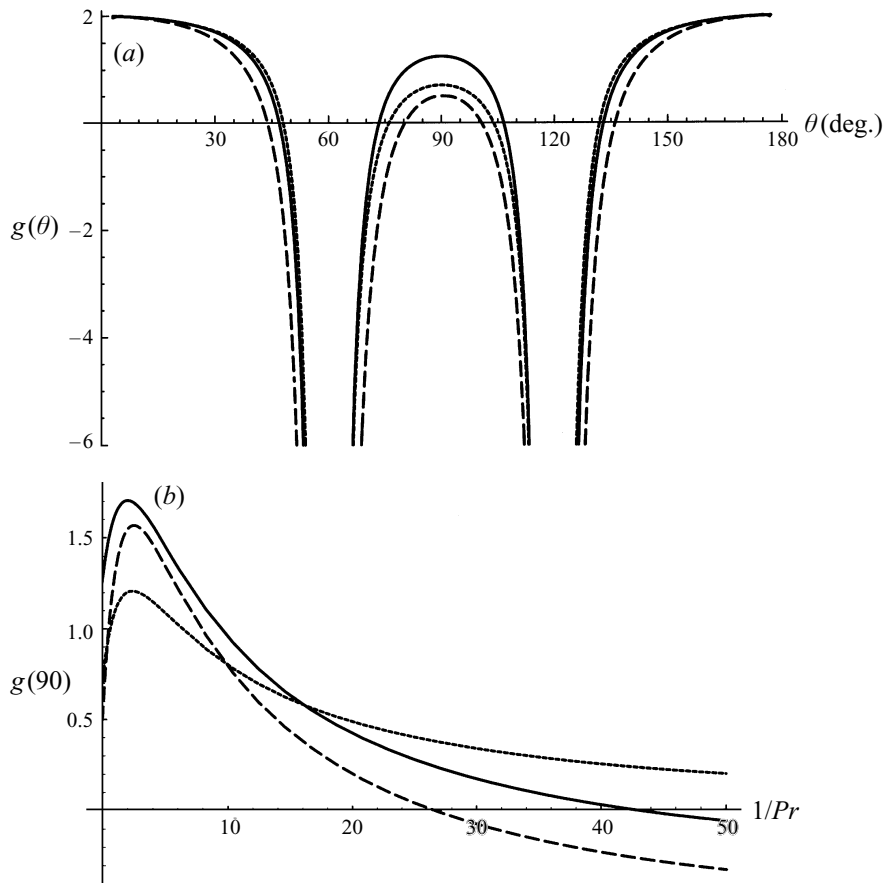
FIGURE 4. Variation of the cubic interaction coefficient (*a*) $g(\theta)$ vs. θ, (*b*) $g(90)$ vs. Pr^{-1}. The solid lines refer to the Pearson solution with $Bi^t = 0$ and $Bi^b \to \infty$. The dashed line corresponds to $Bi^t = 1$ and $Bi^b \to \infty$, and the dotted line corresponds to $Bi^t = 0$ and $Bi^b = 0.01$.

values of Bi for an infinite Prandtl number (figure 4*a*). Figure 4(*b*) shows the value of the cubic interaction term for $\theta = 90°$. As for buoyancy-driven Rayleigh–Bénard convection (Manneville 1990), the preferred pattern is rolls if $g(90) > g_d$ and squares if $g(90) < g_d$. We observe asymptotes for the values of $60°$ and $120°$ which correspond to singularities in the second-order solution (the operator tends to that of the linear problem), hence the need to use the three resonant modes.

6. Relative stability of patterns

With the amplitude equations derived in the previous two sections, we are now able to tackle the problem of pattern selection and relative stability of steady planforms. To study the three usual patterns that could appear above threshold (hexagons, squares and rolls), we will use six complex amplitudes in the horizontal plane (see also Kubstrup *et al.* 1996). The relative orientation of the wavevectors corresponding to the six amplitudes is shown in figure 5. It corresponds to two families of wavevector triads. In the present section, we shall restrict consideration to the local stability of the different stationary perfect patterns. We will not consider here spatial modulation of these patterns but only competition between perfect planforms. We denote with
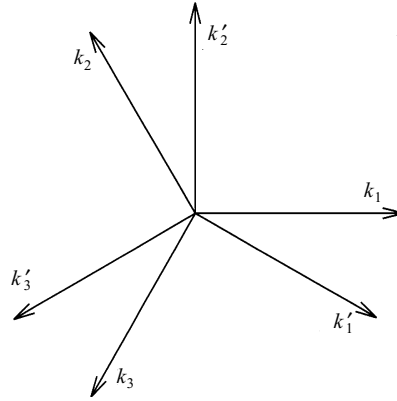
FIGURE 5. Two triads of resonant wavevectors $\boldsymbol{k}_c$ and $\boldsymbol{k}'_c$ in the horizontal plane (x, y) forming an angle of $30°$ one with one other.

g_t and g_n the cubic interaction term $g(\theta)$ with θ equal $30°$ and $90°$, respectively. The amplitude equations for the six complex amplitudes without spatial terms are

$$\left.\begin{aligned}
\partial_t A_1 &= \alpha_l \varepsilon A_1 + \alpha_q A_2^* A_3^* - g_d |A_1|^2 A_1 - g_{nd} \left(|A_2|^2 + |A_3|^2\right) A_1 \\
&\quad - g_t \left(|A_1'|^2 + |A_3'|^2\right) A_1 - g_n |A_2'|^2 A_1, \\
\partial_t A_1' &= \alpha_l \varepsilon A_1' + \alpha_q A_2'^* A_3'^* - g_d |A_1'|^2 A_1' - g_{nd} \left(|A_2'|^2 + |A_3'|^2\right) A_1' \\
&\quad - g_t \left(|A_1|^2 + |A_2|^2\right) A_1' - g_n |A_3|^2 A_1'.
\end{aligned}\right\} \tag{6.1}$$

The equations for A_2, A_3 and A_2', A_3' are obtained by circular permutation of the indices $(1, 2, 3)$ and $(1, 2, 3)'$.

There are two ways to treat the problem of pattern selection. For a variational problem one may use a Lyapunov functional and compare the location and relative size of potential wells as the extrema correspond to the different stationary solutions, with the minima corresponding to locally stable states. Furthermore, the existence of a Lyapunov functional ensures asymptotic stability. Alternatively, we may study the relative stability of patterns by computing the eigenvalues of the linearized system around each solution. In this approach, there is no need of a global Lyapunov functional (Segel 1965; Busse 1967). The local stability of each pattern is also obtained but no information about the size and depth of the potential wells is known, i.e. about the basins of attraction of the different solutions. The relative stability of the convective planforms depends on the distance to the threshold, ε, and on the coefficients of the amplitude equations, hence on the parameters of the problem, as expected.

Take, for instance, the square pattern. We have

$$|A_1|^2 = |A_2'|^2 = \frac{\alpha_l \varepsilon}{g_d + g_n}, \quad \text{otherwise } A_j = 0, A_j' = 0. \tag{6.2}$$

Thus a square pattern is stable, expected only supercritically, when

$$\varepsilon > \frac{\alpha_q^2(g_d + g_n)}{\alpha_l(g_d + g_n - g_{nd} - g_t)^2}, \quad g_{nd} + g_t > g_d + g_n, \quad g_d > g_n. \tag{6.3}$$

Moreover, it can be shown that squares and rolls are mutually excluding patterns (see figure 9*b*) as also found by Kubstrup *et al.* (1996).

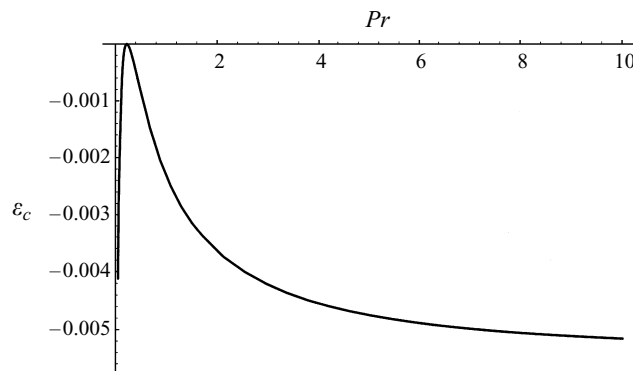For the stability of the hexagons, we make a distinction between the earlier

FIGURE 6. The subcritical range (between the curve and the X-axis) versus Pr,
for $Bi^b \to \infty$ and $Bi^t = 0$.

mentioned up- and down-hexagons. The stability of up-hexagons relative to down-hexagons is linked to the sign of α_q. For $\alpha_q > 0$ the up-hexagons are stable while if $\alpha_q < 0$ the down-hexagons are stable. Let us restrict consideration to the local stability of the up-hexagons (Koschmieder 1993). Note, however, that as α_q appears squared in the expressions that follow, the stability of the down-hexagons obeys the same condition in the corresponding domain $\alpha_q < 0$. For up-hexagons we have

$$|A_j|^2 = \frac{\alpha_q + \left[\alpha_q^2 + 4\alpha_l\,\varepsilon(g_d + 2g_{nd})\right]^{1/2}}{2\,(g_d + 2g_{nd})}, \quad \text{and } A_j' = 0. \tag{6.4}$$

The conditions that ensure the stability of the hexagonal pattern are

$$\varepsilon > -\frac{\alpha_q^2}{4\alpha_l(g_d + 2g_{nd})}, \quad g_d + 2g_{nd} > 0, \quad g_n + 2g_t > 0, \tag{6.5}$$

and two additional conditional inequalities:

$$\text{if } g_{nd} > g_d \text{ then } \varepsilon < \frac{\alpha_q^2\,(2g_d + g_{nd})}{\alpha_l(g_{nd} - g_d)^2} \tag{6.6}$$

and

$$\text{if } g_d + 2g_{nd} > g_n + 2g_t \text{ then } \varepsilon < \frac{\alpha_q^2\,(2g_t + g_n)}{\alpha_l(g_d + 2g_{nd} - g_n - 2g_t)^2}. \tag{6.7}$$

For the hexagons, there is a range of subcritical stability. For $\varepsilon < 0$, there is coexistence between the motionless conduction state (all amplitudes vanish) and the hexagonal structure, hence hysteretic behaviour near the instability threshold. Yet, the computed values shown in figure 6 indicate that this region is quite narrow thus justifying the scaling used in this paper (see §4).

Another interesting question is the problem of quasi-patterns (Malomed, Nepomnyashchy & Tribelsky 1989). For the above six coupled amplitude equations, there is also a stationary solution with all amplitudes equal, hence

$$|A_j|^2 = |A_j'|^2 = \frac{\alpha_q + \left[\alpha_q^2 + 4\alpha_l\,\varepsilon(g_d + 2g_{nd} + 2g_t + g_n)\right]^{1/2}}{2\,(g_d + 2g_{nd} + 2g_t + g_n)}. \tag{6.8}$$

The quasi-pattern planform in this case is shown in figure 7, where it appears as a penta-dodecagonal structure. This pattern does not satisfy the condition of closed
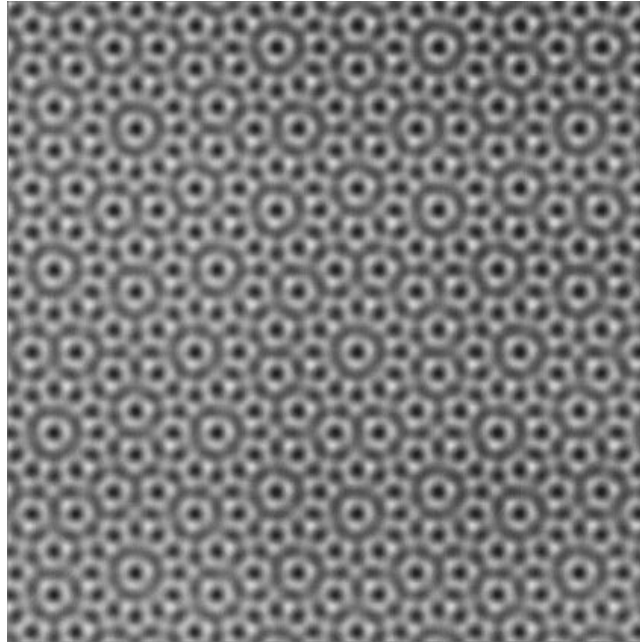
FIGURE 7. The quasi-pattern obtained with the six amplitudes equal. The constant amplitudes are modulated by the critical wavenumber along each wavevector. The size of the container corresponds to 16×16 wavelengths.
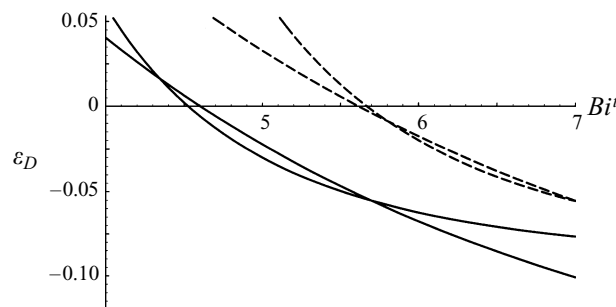

FIGURE 8. The local stability of the quasi-pattern for $Bi^b \to \infty$. The pattern is stable in the region in between the curves. The solid lines correspond to $Pr \to \infty$ and the dashed lines to $Pr = 7$.

convective cells, and it may seldom appear in experiments. It has been observed in the Faraday parametric excitation experiment (Edwards & Fauve 1993). Following the same scheme used to assess the local stability of (regular) patterns we have studied the local stability of the quasi-pattern. Figure 8 depicts the stability conditions found for $Bi^b \to \infty$ and varying Bi^t. The quasi-pattern is stable between the curves. The stability domain of the quasi-patterns appears quite narrow indeed.

For illustration, we provide a few plots. A plot locating the stable patterns in the parameter space may be drawn (phase-like diagram). Figure 9(*a*) shows the stable patterns for $Bi^t = 0.38$, $Pr \to \infty$ and varying Bi^b (the subcritical domain between the motionless state and the hexagonal convective state is so narrow that it does not appear in this figure). It shows coexistence of hexagons and squares for intermediate values of the bifurcation parameter ε. For this value of Bi^t that corresponds to
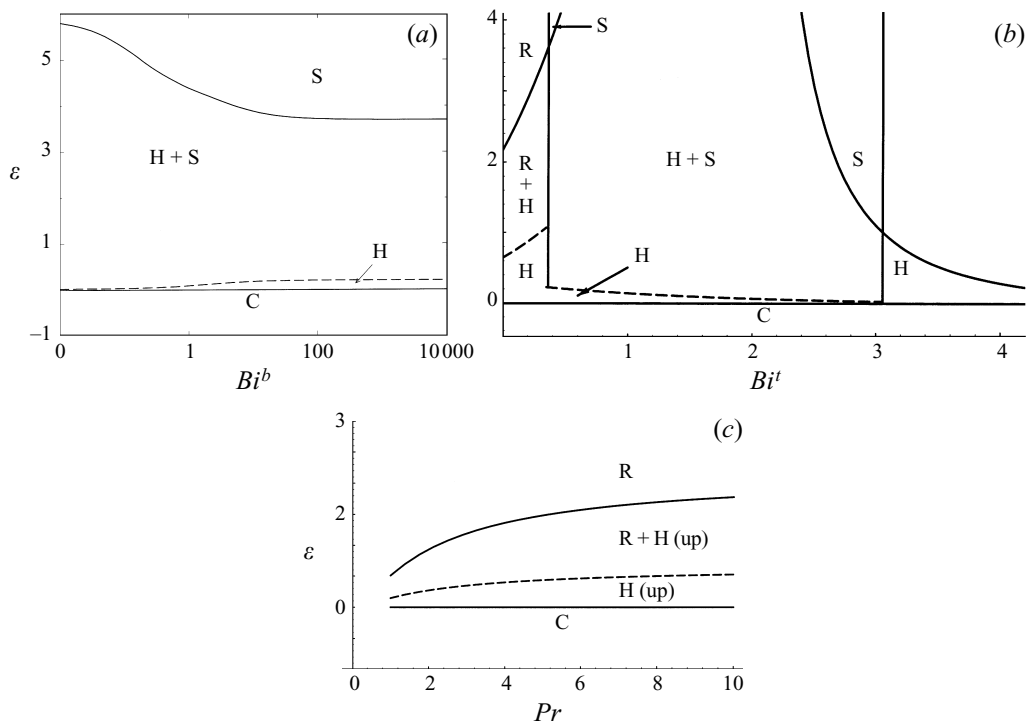
FIGURE 9. Plot of the local stability of the different patterns: (*a*) hexagons H and squares S for $Bi^t = 0.38$, $Pr \to \infty$; (*b*) rolls R for $Bi^b \to \infty$, $Pr \to \infty$; (*c*) for $Bi^b \to \infty$, $Bi^t = 0$. The dashed lines correspond to hysteretic transitions.

usual experiments (Koschmieder 1993) we cannot find stable rolls patterns. Thus upon increasing the value of ε, we cross two coexistence domains. First we cross the coexistence region between the motionless state and hexagons and later the coexistence region between the hexagon and the square pattern. Figure 9(*b*) shows the stable patterns for $Bi^b \to \infty$, $Pr \to \infty$ and varying Bi^t which appears when changing the depth of the overlying air layer (2.10). In figure 9(*b*) we cannot find rolls for $Bi^t > 0.36$: this last inequality is always satisfied in the experiments so far performed. This justifies why in standard Bénard experiments a secondary transition from hexagons to rolls is not observed but rather a transition from hexagons to squares is found (Nitschke & Thess 1995). Figure 9(*c*) shows the stable patterns for $Bi^b \to \infty$, $Bi^t = 0$ and varying Pr. Our findings corroborate the result of Thess & Bestehorn (1995) that predict a transition from up- to down-hexagons through an intermediate rolls state by lowering Pr. Figure 9(*c*) corresponds to $Pr > Pr^*$, where up-hexagons are stable. The region where up-hexagons are stable shrinks to zero when Pr is reduced to Pr^*. The use of six amplitudes has permitted a comparison of the stability of hexagons, squares and rolls.

7. Numerical simulations

The aim of this section is to complete the analytical findings with the numerical results obtained by integrating (4.16). Rather than integrating only one family of equations (4.16), we integrate two families to allow for the possibility of obtaining
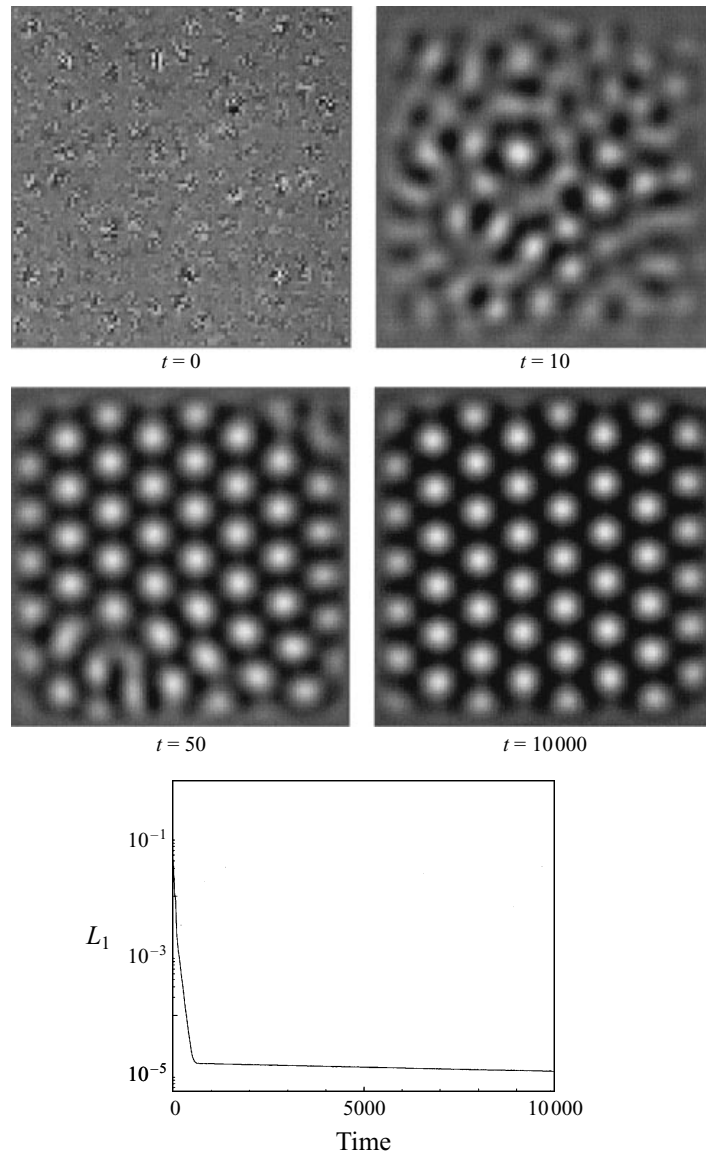
$t = 0$ $t = 10$

$t = 50$ $t = 10\,000$

FIGURE 10. Time evolution starting from a random initial condition toward an hexagonal structure, with $\varepsilon = 0.063, \beta_i = 0$. How the initial condition relaxes toward the final steady state is illustrated by the evolution of the norm L_1. The values of the coefficients entering the amplitude equations are those given in (4.16) with $Pr \to \infty$.

hexagons, squares and rolls. For this purpose we add cubic interaction terms between these two families of equations (see §5).

We have used a finite difference method with a semi-implicit scheme (second order in space and first order in time). The details of the method can be found in Christov, Pontes & Velarde (1996). We followed the time evolution of the patterns by monitoring a norm that measures the distance between two successive pictures of the convective state of the system, hence a norm sensitive to both amplitude and phase variations.
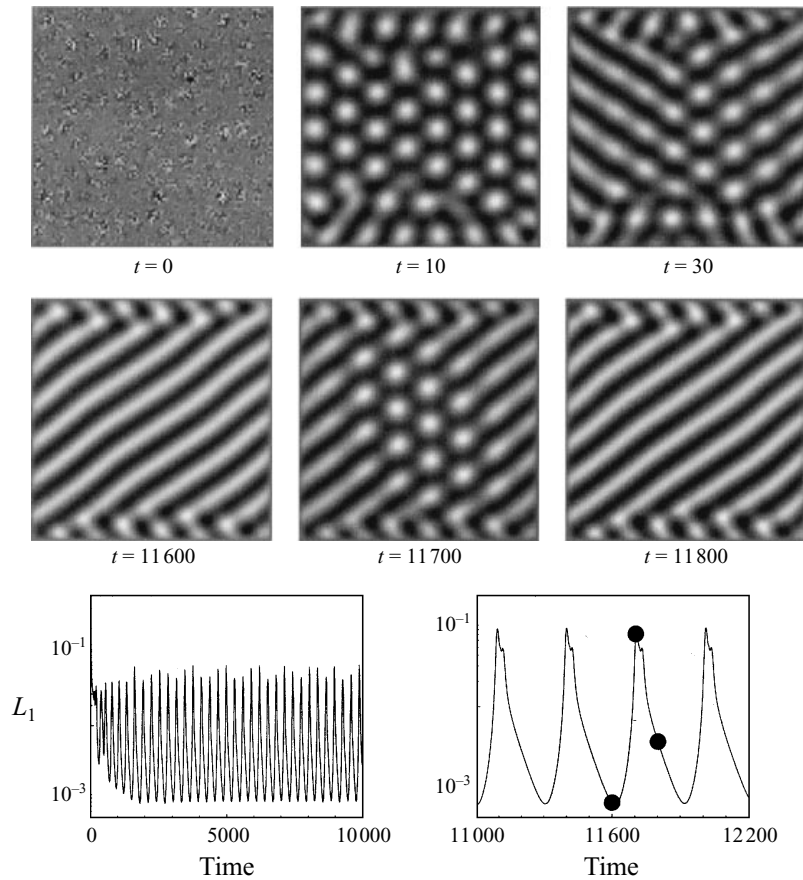
FIGURE 11. Pulsating evolution (rolls-hexagons) with $\varepsilon = 0.63$, starting from a random initial condition. The norm L_1 exhibits the periodicity with time. The values of the coefficients entering the amplitude equations are those given in (4.16) with $Pr \to \infty$.

The norm is

$$L_1 = \frac{1}{\Delta t} \frac{\sum_{i,j,p} |A_p^{n+1}(i,j) - A_p^n(i,j)|}{\sum_{i,j,p} |A_p^{n+1}(i,j)|}, \tag{7.1}$$

where the sums run over the i and j points of the spatial grid, and n is the time counter. If a steadily decaying value of L_1 follows the dynamic evolution until a constant value is reached, then the system settles in a steady state. Note, however, that this may not always be the case due to the non-variational terms in (4.16). At the lateral boundaries of the square container, we impose

$$A_p = 0, \tag{7.2}$$

hence no motion at the rigid lateral walls.

Figure 10 displays the time evolution of the reconstructed horizontal temperature field from the amplitudes

$$T(x, y, t) \propto \sum_p A_p \exp(i\boldsymbol{k}^{(p)} \cdot \boldsymbol{r}) + \text{c.c.}$$

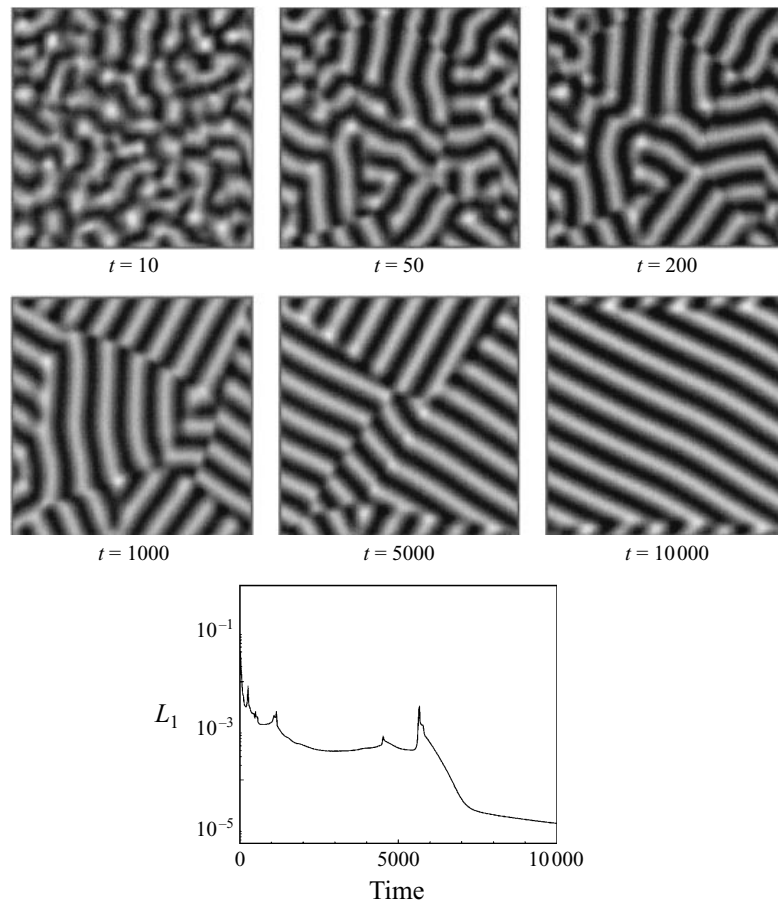The computation was performed in a square geometry with eight critical wavelengths

FIGURE 12. Time evolution starting from a random initial condition toward a roll structure with $\varepsilon = 2.52, \beta_i = 0$. How the initial condition relaxes toward the final state is illustrated by the evolution of the norm L_1. The values of the coefficients entering the amplitude equations are those given in (4.16) with $Pr \to \infty$.

as sidelength and $\varepsilon = 0.063, \beta_i = 0$ (variational case). The time evolution of the norm L_1 shows that we reach a stationary state. A similar situation occurs for the same parameters except that $\beta_i \neq 0$ (values given by (4.16) for $Pr \to \infty$). We also observe a monotonic decay to a steady state.

Figure 11 corresponds to $\varepsilon = 0.63$ and $\beta_i \neq 0$. The hexagons are no longer stable and a roll structure appears. However the latter does not settle as pulsating hexagons periodically destabilize the roll pattern.

Figure 12 shows the time evolution towards the roll structure that settles only for large enough supercriticality. Here in both cases, $\beta_i = 0$ and $\beta_i \neq 0$, the system monotonically evolves towards a final, steady state of rolls. Worth mentioning is that the rate of convergence to a steady state is faster in the non-variational case than in the variational one. A variational dynamics appears having a higher structural rigidity of its phase space thus increasing the relaxation time towards a steady state.

Figure 13 illustrates the formation of a square pattern. Square patterns have been observed by White (1988) (temperature-dependent viscosity) and Koschmieder & Prahl (1990) (Bénard–Marangoni convection in small-aspect-ratio containers) and
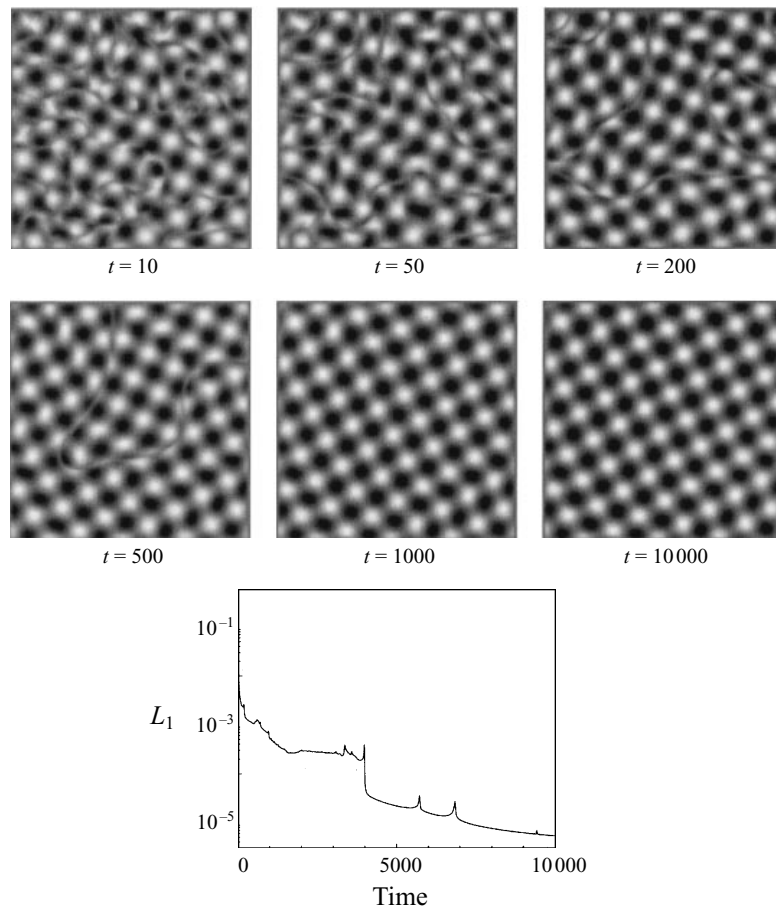
FIGURE 13. Time evolution starting from a random initial condition toward a square pattern with $\varepsilon = 2, \beta_i \neq 0$. How the initial condition relaxes toward the final steady state is illustrated by the evolution of the norm L_1. The values of the coefficients entering the amplitude equation (4.16) correspond to $Bi^t = 2, Bi^b \to \infty$ and $Pr \to \infty$.

recently, as the result of a secondary instability of the hexagons, by Nitschke & Thess (1995). It has been demonstrated that the effect of the lateral walls plays a crucial role in the selection of the planform especially for a small-aspect-ratio container (Dauby & Lebon 1996). In our case, it is the finite Biot number at the top interface that leads to the appearance of such a square pattern (see figure 9*b*).

8. Eckhaus instability

In this section, we study the Eckhaus instability of an hexagonal pattern by using three coupled amplitude equations (4.16). Our study generalizes some earlier works (Caroli, Caroli & Roulet 1984; Sushchik & Tsimring 1994; Hoyle 1995). It is known that one of the mechanisms of instability of an hexagonal pattern in Bénard–Marangoni convection is the Eckhaus instability. It corresponds to the growth of wavenumber modulations and leads to a change of the initial wavenumber towards the optimal value. Physically, the Eckhaus instability is responsible for the creation and annihilation of convective cells, either rolls or hexagons, at a fixed, constant

value of the thermal gradient. The Eckhaus band of stability in the parameter space is found analytically from the phase approximation of the amplitude equations (4.16). The interest of our study rests on the understanding of the role of the non-variational terms, $\beta_i \neq 0$.

A perfect hexagonal pattern is constructed from three rolls with wavevectors satisfying the resonance condition

$$\boldsymbol{k}_c^{(1)} + \boldsymbol{k}_c^{(2)} + \boldsymbol{k}_c^{(3)} = \boldsymbol{0}.$$

Let us start with off-critical wavenumbers $k^{(1)} = k^{(2)} = k^{(3)} \neq k_c$, and $k - k_c = k_d$. The 'modified' amplitude equations that govern the dynamics of this hexagonal pattern are obtained from (4.16) by the following procedure. The first step consists in introducing a change of function in (4.16). We set

$$A_p = A_p' \exp(i\boldsymbol{k}_d^{(p)} \cdot \boldsymbol{r}). \tag{8.1}$$

Then, we write the equations in new Cartesian coordinates orthogonal and parallel to the three rolls axes (X_p), respectively. We rescale space, time, and amplitude as follows:

$$A_p' = c_A A_p''; \quad t'' = c_t t; \quad X_p = c_x x_p; \quad Y_p = c_x y_p. \tag{8.2}$$

If we choose

$$c_A = \frac{\alpha_q}{g_d}; \quad c_t = \frac{\alpha_q^2}{g_d \alpha_t}; \quad c_x = \frac{\alpha_q}{k_c (g_d \alpha_d)^{1/2}}, \tag{8.3}$$

and if we set

$$\beta_1'' = \frac{k_c c_x}{g_d c_A} \beta_1; \quad \beta_2'' = \frac{k_c c_x}{g_d c_A} \beta_2; \quad \gamma = \frac{g_{nd}}{g_d}; \quad \mu = \frac{g_d \alpha_l}{\alpha_q^2} \varepsilon; \quad K = \frac{k_d}{c_x} \tag{8.4}$$

omitting the double prime, the equation (4.16) becomes

$$\begin{aligned}
\partial_t A_1 = {} & \mu A_1 + A_2^* A_3^* + (iK + \partial_{X_1})^2 A_1 - |A_1|^2 A_1 - \gamma \left(|A_2|^2 + |A_3|^2\right) A_1 \\
& + i\beta_1 \left[A_3^* \left(-iK + \partial_{X_2}\right) A_2^* + A_2^* \left(-iK + \partial_{X_3}\right) A_3^*\right] \\
& + i\beta_2 \left[A_2^* \left(\frac{iK}{2} + \partial_{X_2}\right) A_3^* + A_3^* \left(\frac{iK}{2} + \partial_{X_3}\right) A_2^*\right], \tag{8.5}
\end{aligned}$$

and similar equations for A_2 and A_3, obtained by circular permutation of the indices.

As already stated, relative to earlier works (Caroli *et al.* 1984; Sushchik & Tsimring 1994), we have in our problem terms with coefficients β_1 and β_2 that make it non-variational. The stationary homogeneous solution of (8.5) for hexagons is

$$A_p = A_0 \equiv \frac{[1 + (2\beta_1 - \beta_2)K] \pm \left\{[1 + (2\beta_1 - \beta_2)K]^2 + 4(\mu - K^2)(1 + 2\gamma)\right\}^{1/2}}{2(1 + 2\gamma)},$$
$$p = 1, 2, 3. \tag{8.6}$$

In §6 we showed that the solution with the minus sign is stable only for very low values of the Prandtl number, hence we only consider the solution with the plus sign. Needless to say for the case with the minus sign we can follow the same procedure. In particular, we study the stability of the off-critical hexagonal solution to long-wave disturbances (with non-dimensional wavenumber $Q \ll 1$, see (8.12)). Thus we assume that the so-called phase approximation $(Q \to 0)$ is valid.

We add small perturbations to the regular hexagonal pattern in the form

$$A_p = (A_0 + a_p) \exp(i\phi_p), \quad p = 1, 2, 3, \tag{8.7}$$

and $a_p(\mathbf{r}, t), |\nabla\phi_p(\mathbf{r}, t)| \ll 1$. Substitution of (8.7) into (8.5) and linearization with respect to small perturbations of amplitudes and phases leads to the following equations:

$$\partial_t a_p = -\left\{[1 + (2\beta_1 - \beta_2)K + 2A_0] A_0 - \partial^2_{X_p}\right\}a_p + [1 + (2\beta_1 - \beta_2)K - 2\gamma A_0] A_0(a_j + a_k)$$
$$-2KA_0\partial_{X_p}\phi_p + \beta_1 A_0^2 \left[\partial_{X_j}\phi_j + \partial_{X_k}\phi_k\right] + \beta_2 A_0^2 \left[\partial_{X_j}\phi_k + \partial_{X_k}\phi_j\right], \qquad (8.8)$$

$$\partial_t \phi_p = -[1 + (2\beta_1 - \beta_2)K] A_0(\phi_p + \phi_j + \phi_k) + \partial^2_{X_p}\phi_p + 2KA_0^{-1}\partial_{X_p}a_p$$
$$+\beta_1 \left[\partial_{X_j}a_j + \partial_{X_k}a_k\right] + \beta_2 \left[\partial_{X_j}a_k + \partial_{X_k}a_j\right]. \qquad (8.9)$$

For long-wave perturbations and for sufficiently low values of the forcing μ (proportional to ε), i.e. in the domain where the hexagons are stable to spatially homogeneous disturbances (§6), time and space derivatives of amplitudes a_p in (8.8) are of higher order in Q and can be neglected in the phase approximation. Then (8.8) become algebraic relations between a_p and phase gradients. Thus we have

$$a_p = \lambda\partial_{X_p}\phi_p + \beta\partial_{X_j}\phi_j + \beta\partial_{X_k}\phi_k + \delta\partial_{X_k}\phi_j + \delta\partial_{X_j}\phi_k + \rho\partial_{X_p}\phi_k + \rho\partial_{X_p}\phi_j + \rho\partial_{X_k}\phi_p + \rho\partial_{X_j}\phi_p, \qquad (8.10)$$

with

$$\lambda = \frac{(1-b)c - 2c_1}{(b+1)(b-2)}; \quad \beta = \frac{-(c + b\,c_1)}{(b+1)(b-2)}; \quad \delta = \frac{(1-b)c_2}{(b+1)(b-2)}; \quad \rho = \frac{-c_2}{(b+1)(b-2)};$$

and

$$b = \frac{1 + 2A_0}{1 + (2\beta_1 - \beta_2)K - 2\gamma A_0}; \quad c = \frac{2K}{1 + (2\beta_1 - \beta_2)K - 2\gamma A_0};$$

$$c_i = \frac{-\beta_i A_0}{1 + (2\beta_1 - \beta_2)K - 2\gamma A_0}, \quad i = 1, 2.$$

After substitution of (8.10) into (8.9) we get in compact form

$$\partial_t \phi = \mathrm{L}\phi, \qquad (8.11)$$

where L is a differential operator acting on a vector ϕ. Looking for marginal stability of this system of phase equations, we substitute the plane wave solution

$$\phi_p = P_p \exp(\mathrm{i}\mathbf{Q} \cdot \mathbf{R} + \sigma t) \qquad (8.12)$$

with ($\mathbf{R} = \{X, Y\}$), and compute the three eigenvalues of the operator. At the lowest order in Q we get

$$\sigma_1 = -3a + O[Q^2],$$
$$\sigma_2 = \left[-\tfrac{1}{4} + KA_0^{-1}(\tfrac{1}{2}\beta + \rho - \delta - \tfrac{1}{2}\lambda) + (\beta_2 - \tfrac{1}{2}\beta_1)(\tfrac{1}{2}\beta + \rho - \delta - \tfrac{1}{2}\lambda)\right] Q^2,$$
$$\sigma_3 = \left[-1 + KA_0^{-1}(4\rho - 2\beta - 2\lambda) + \beta_1(\beta + \lambda - 2\rho) + 2\beta_2(\beta - \delta)\right] \tfrac{3}{4}Q^2,$$

with $a = [1 + (2\beta_1 - \beta_2)K] A_0 > 0$. Contrary to the variational case the matrix of the eigenvalue problem is no longer Hermitian, hence its eigenvalues may be complex numbers and the stability of the solution A_0 demands that $\mathrm{Re}[\sigma_p] < 0$. The Eckhaus band corresponds to the region of the (K, μ)-plane where the solution A_0 is stable to long-wave perturbations. In figure 14, we plot the Eckhaus band for positive, negative and vanishing β_i, respectively. Note that due to the fact that the β_i terms yield a non-Hermitian matrix, the eigenvalues may be complex, hence leading to an oscillatory Eckhaus instability. However, for the parameter range of values used in our work, we have not observed such oscillatory instability.
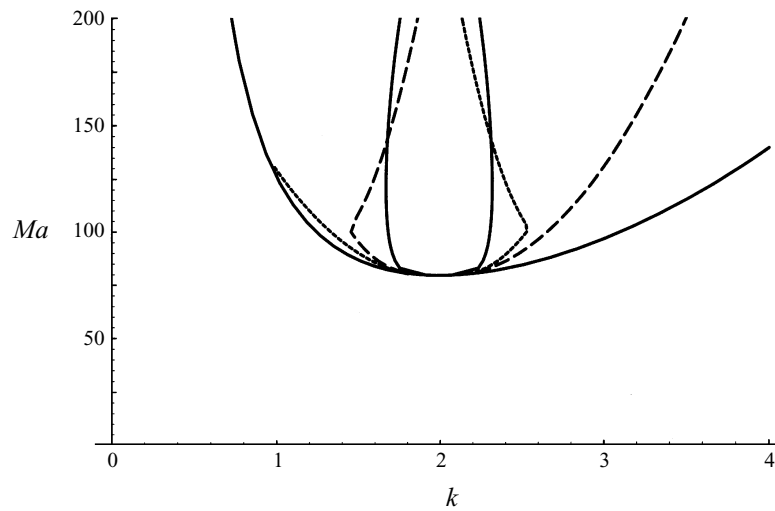
FIGURE 14. Eckhaus band in the (k, Ma)-plane (homomorphic to the (K, μ)-plane). For $\beta_i = 0$ (case A), the hexagons are Eckhaus stable between the two solid lines; $\beta_1 = -0.345, \beta_2 = -1.4$ (case B) stable between the two broken lines; $\beta_1 = 0.345, \beta_2 = 1.4$ (case C) stable between the dotted lines. The marginal stability curve is also displayed. All curves were obtained for $\gamma = 1.36$.

It appears that non-zero values of β_i lead to a widening of the Eckhaus band. The band of allowed wavenumbers has significantly grown relative to the case of vanishing β_i. It is also interesting to note that the curves are symmetric around K for the transformation $\beta_1 = -\beta_1$ and $\beta_2 = -\beta_2$. This result does not appear from the simple inspection of the formula and may not be valid for other values of β_i.

Figure 15 shows the results of numerical integration of (8.5), starting from random initial conditions and off-critical wavenumber ($k_d = 0.8, Ma = 120$). We see the emergence of the hexagonal pattern with some defects and joint grains. The evolution of the phase and modulus of A_1 is also displayed. The time scale of the phase dynamics is much longer than the time scale of the dynamics of the modulus alone hence justifying the validity of the phase approximation.

9. Conclusions

Amplitude equations for hexagonal planforms and for convective patterns with two modes forming an arbitrary angle in the surface-tension-gradient-driven Bénard–Marangoni convection problem have been derived. These amplitude equations de-scribe the pattern dynamics for weakly supercritical flows. We have obtained the steady solutions of the amplitude equations that correspond to rolls, hexagons and squares, and studied their local stability. A plot giving the local stability of these structures as functions of the parameters of the system (Bi^t, Bi^b and Pr) has been produced, and the results have been compared to available experimental data. Past the onset of instability, the hexagonal structure with fluid rising in the centre of the cells is selected in agreement with all available experimental results (Koschmieder 1993). For higher supercritical values, coexistence between patterns is predicted in agreement with a recent experimental result where squares were obtained high above threshold (Nitschke & Thess 1995). We have also found quasi-patterns with, however, quite a narrow stability domain.

The numerical integration of the amplitude equations supports the analytical pre-
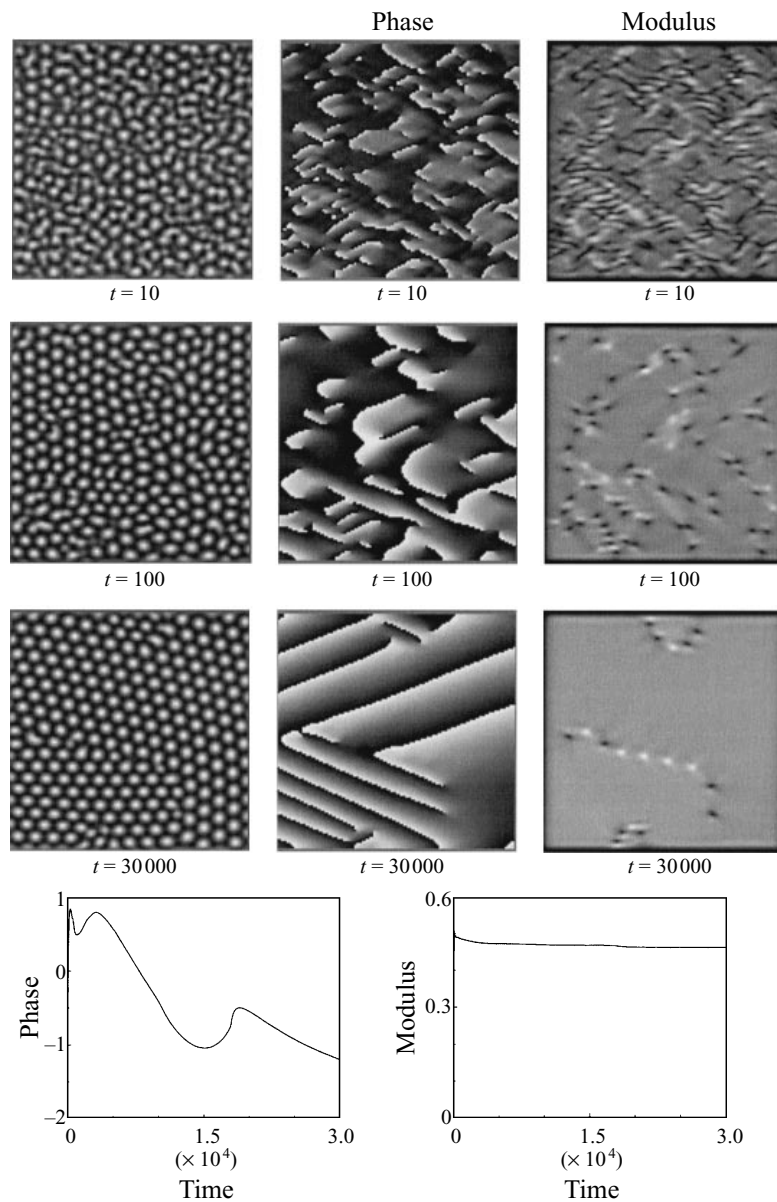
FIGURE 15. Time evolution from a random initial condition ($t = 0$) of an hexagonal structure with $\beta_i = 0$, $\gamma = 1.36$, $k_d = 0.8$, $Ma = 120$.

dictions and has permitted us to highlight the role of the non-variational terms involved in the dynamics of pattern formation in Bénard–Marangoni convection. On the one hand, relative to the variational case we have observed a faster convergence towards a final steady state if it is asymptotically ($t \to \infty$) reached. On the other hand, we have shown that there are cases where a steady state may not occur due to the non-variational character of the dynamics. Our numerical study justifies the use of the phase approximation in the analytical prediction of the Eckhaus stable band for the hexagonal pattern. A novel result is that non-variational terms in the dynamics

break the symmetry around k_c of the Eckhaus band of allowable modes; however this band is too wide to select a single wavenumber above threshold.

Appendix A. Linear adjoint problem

In this Appendix, we determine the linear adjoint problem and its solution. We have

$$\langle \boldsymbol{u}^+, \mathrm{L}(\boldsymbol{u}) \rangle = \langle \boldsymbol{u}, \mathrm{L}^+(\boldsymbol{u}^+) \rangle, \tag{A 1}$$

$$\boldsymbol{u}^T = \left[w, T, T|_{z=1} \right], \tag{A 2}$$

$$\boldsymbol{u}^{+T} = \left[w^+, T^+, \partial_z w^+|_{z=1} \right]. \tag{A 3}$$

A scalar product is introduced

$$\langle \boldsymbol{a}, \boldsymbol{b} \rangle = \lim_{L \to \infty} \frac{1}{L^2} \int_{-L}^{+L} \int_{-L}^{+L} \mathrm{d}x \mathrm{d}y \left[\overline{a_3} b_3 + \int_0^1 (\overline{a_1} b_1 + \overline{a_2} b_2) \mathrm{d}z \right]. \tag{A 4}$$

By integrating by parts we get the linear adjoint problem and corresponding boundary conditions

$$\left(\mathrm{D}^2 - k^2 \right)^2 W^+(z) + T^+(z) = 0, \tag{A 5}$$

$$\left(\mathrm{D}^2 - k^2 \right) T^+(z) = 0; \tag{A 6}$$

at $z = 0$

$$W^+ = 0; \quad \mathrm{D}W^+ = 0; \quad \mathrm{D}T^+ - Bi^b T^+ = 0, \tag{A 7}$$

and at $z = 1$

$$W^+ = 0; \quad \mathrm{D}^2 W^+ = 0; \quad \mathrm{D}T^+ + Bi^t T^+ - k^2 Ma_c \mathrm{D}W^+ = 0. \tag{A 8}$$

For arbitrary values of the parameters, the solution of these equations is found using the ODE Wolfram (1993) routine for symbolic integration. The normalization adopted for the adjoint solution is

$$\int_0^1 W^+(z) \, \mathrm{d}z = 1. \tag{A 9}$$

Appendix B. Second-order solution (hexagons)

The solution to the second order in δ is found as follows:
(i) Solution proportional to $\left[A_1^2 \exp(2\mathrm{i}\boldsymbol{k}^{(1)} \cdot \boldsymbol{r}) + A_2^2 \exp(2\mathrm{i}..^{(2)}) + A_3^2 \exp(2\mathrm{i}..^{(3)}) + \mathrm{c.c.} \right]$

$$\left(\mathrm{D}^2 - 4k^2 \right) T_2(z) + W_2(z) = W\mathrm{D}T - T\mathrm{D}W. \tag{B 1}$$

$$\left(\mathrm{D}^2 - 4k^2 \right)^2 W_2(z) = 2Pr^{-1} \left[W\mathrm{D}^3 W - \mathrm{D}W\mathrm{D}^2 W \right], \tag{B 2}$$

and the boundary condition (the others are unchanged) in $z = 1$

$$\mathrm{D}^2 W_2 + 4k^2 \, Ma_c \, T_2 = 0. \tag{B 3}$$

For the horizontal velocity we solve

$$\left(\nabla_{1x}^2 \boldsymbol{u}_2^H + \partial_z \nabla_{1x} w_2\right) = \boldsymbol{0} \tag{B 4}$$

to obtain

$$\boldsymbol{u}_2^H = \frac{\mathrm{D} W_2}{4k^2} \nabla_{1x} \left[A_1^2 \exp(2\mathrm{i}\boldsymbol{k}^{(1)} \cdot \boldsymbol{r}) + A_2^2 \exp(2\mathrm{i}..^{(2)}) + A_3^2 \exp(2\mathrm{i}..^{(3)}) + \mathrm{c.c.}\right]. \tag{B 5}$$

(ii) Solution proportional to $\left[|A_1|^2 + |A_2|^2 + |A_3|^2\right]$ (zero mode)

$$\mathrm{D}^2 T_0 + W_0 = W\mathrm{D}T + T\mathrm{D}W, \tag{B 6}$$

$$\mathrm{D}^4 W_0 = 0, \tag{B 7}$$

and the boundary condition at $z = 1$

$$\mathrm{D}^2 W_0 = 0. \tag{B 8}$$

Thus, there is no velocity for the zero mode.

(iii) Solution proportional to

$$\left[A_1 A_2^* \exp(\mathrm{i}(\boldsymbol{k}^{(1)} - \boldsymbol{k}^{(2)}) \cdot \boldsymbol{r}) + A_1 A_3^* \exp(\mathrm{i}..^{(1)-(3)}) + A_2 A_3^* \exp(\mathrm{i}..^{(2)-(3)}) + \mathrm{c.c.}\right]$$

$$\left(\mathrm{D}^2 - 3k^2\right) T_3(z) + W_3(z) = 2W\mathrm{D}T - T\mathrm{D}W, \tag{B 9}$$

$$\left(\mathrm{D}^2 - 3k^2\right)^2 W_3(z) = 3Pr^{-1} \left[W\mathrm{D}^3 W - k^2 W\mathrm{D}W\right], \tag{B 10}$$

and the boundary condition at $z = 1$

$$\mathrm{D}^2 W_3 + 3k^2 Ma_c T_3 = 0. \tag{B 11}$$

For the horizontal velocity we have

$$\boldsymbol{u}_3^H = \frac{\mathrm{D} W_3}{3k^2} \nabla_{1x} \Big[A_1 A_2^* \exp(\mathrm{i}(\boldsymbol{k}^{(1)} - \boldsymbol{k}^{(2)}) \cdot \boldsymbol{r})$$
$$+ A_1 A_3^* \exp(\mathrm{i}..^{(1)-(3)}) + A_2 A_3^* \exp(\mathrm{i}..^{(2)-(3)}) + \mathrm{c.c.}\Big].$$

The last system we need to solve is proportional to the k-mode (resonant term). This is achieved using the solvability condition (Fredholm alternative).

(iv) Solution proportional to $\exp(\mathrm{i}\boldsymbol{k}^{(1)} \cdot \boldsymbol{r})$ (the solution proportional to : $\exp(-\mathrm{i}..^{(1)})$ is the c.c., and similarly for the amplitudes $A_2 ; A_3$)

$$\left(\mathrm{D}^2 - k^2\right) T_{21}(z) + W_{21}(z) = (2W\mathrm{D}T + T\mathrm{D}W)A_2^* A_3^* - 2\mathrm{i}T\left(\boldsymbol{k}^{(1)} \cdot \nabla_{1X}\right) A_1, \tag{B 12}$$

$$\left(\mathrm{D}^2 - k^2\right)^2 W_{21}(z) = Pr^{-1} \left[W\mathrm{D}^3 W + 2\mathrm{D}W\mathrm{D}^2 W - 3k^2 W\mathrm{D}W\right] A_2^* A_3^*$$
$$- 4\mathrm{i}\left(\mathrm{D}^2 W - k^2 W\right)\left(\boldsymbol{k}^{(1)} \cdot \nabla_{1X}\right) A_1, \tag{B 13}$$

and the boundary condition at $z = 1$

$$\mathrm{D}^2 W_{21} + k^2 Ma_c T_{21} = -k^2 Ma^{(1)} T A_1 + 2\mathrm{i}Ma_c T\left(\boldsymbol{k}^{(1)} \cdot \nabla_{1X}\right) A_1. \tag{B 14}$$

For the horizontal velocity we have

$$\left(\nabla_{1x}^2 + \partial_{z^2}\right)\left(\nabla_{1x}^2 \boldsymbol{u}_{21} + \partial_z \nabla_{1x} w_{21}\right) = \left(\mathrm{D}^3 W - k^2 \mathrm{D}W\right) \left[2\frac{\boldsymbol{k}^{(1)}}{k^2}\left(\boldsymbol{k}^{(1)} \cdot \nabla_{1X}\right) A_1 - \nabla_{1X} A_1\right].$$

Appendix C. Second-order solution (2 modes)

The systems proportional to $\left[A_1^2 \exp(2\mathrm{i}k^{(1)} \cdot r) + A_2^2 \exp(2\mathrm{i}..^{(2)}) + \text{c.c.}\right]$ and proportional to $\left[|A_1|^2 + |A_2|^2\right]$ (zero mode) are the same as for the hexagons.

(i) Solution proportional to

$\left[A_1 A_2^* \exp(\mathrm{i}(k^{(1)} - k^{(2)}) \cdot r) + \text{c.c.}\right]$ (modulus $k\gamma^{1/2} = k(2 - 2\beta)^{1/2}$)

$$\left(\mathrm{D}^2 - \gamma k^2\right) T_\gamma(z) + W_\gamma(z) = 2\beta T \mathrm{D}W + 2W\mathrm{D}T, \tag{C 1}$$

$$\left(\mathrm{D}^2 - \gamma k^2\right)^2 W_\gamma(z) = 2Pr^{-1}\left[(1 - \beta)W\mathrm{D}^3 W + (1 - \beta + \beta\gamma)\mathrm{D}W\mathrm{D}^2 W\right.$$
$$\left. - \gamma(1 + \beta)k^2 W\mathrm{D}W\right], \tag{C 2}$$

and the boundary condition at $z = 1$

$$\mathrm{D}^2 W_\gamma + \gamma k^2 Ma_c T_\gamma = 0. \tag{C 3}$$

For the horizontal velocity we have

$$u_\gamma^H = \frac{\mathrm{D}W_\gamma}{\gamma k^2}\nabla_{1x}\left[A_1 A_2^* \exp(\mathrm{i}(k^{(1)} - k^{(2)}) \cdot r) + \text{c.c.}\right].$$

(ii) Solution proportional to

$\left[A_1 A_2 \exp(\mathrm{i}(k^{(1)} + k^{(2)}) \cdot r) + \text{c.c.}\right]$ (modulus $k\alpha^{1/2} = k(2 + 2\beta)^{1/2}$)

$$\left(\mathrm{D}^2 - \alpha k^2\right) T_\alpha(z) + W_\alpha(z) = 2W\mathrm{D}T - 2\beta T\mathrm{D}W, \tag{C 4}$$

$$\left(\mathrm{D}^2 - \alpha k^2\right)^2 W_\alpha(z) = 2Pr^{-1}\left[(1 + \beta)W\mathrm{D}^3 W + (1 + \beta - \beta\alpha)\mathrm{D}W\mathrm{D}^2 W\right.$$
$$\left. - \alpha(1 - \beta)k^2 W\mathrm{D}W\right], \tag{C 5}$$

and the boundary condition at $z = 1$

$$\mathrm{D}^2 W_\alpha + \alpha k^2 Ma_c T_\alpha = 0. \tag{C 6}$$

For the horizontal velocity we have

$$u_\alpha^H = \frac{\mathrm{D}W_\alpha}{\alpha k^2}\nabla_{1x}\left[A_1 A_2 \exp(\mathrm{i}(k^{(1)} + k^{(2)}) \cdot r) + \text{c.c.}\right]$$

The last system we need to solve is proportional to the k-mode (resonant term). Once more, we need to use the solvability condition to get a solution (Fredholm alternative).

(iii) Solution proportional to $\exp(\mathrm{i}k^{(1)} \cdot r)$ (The solution proportional to $\exp(-\mathrm{i}..^{(1)})$ is the c.c., and similarly for the amplitude A_2)

$$\left(\mathrm{D}^2 - k^2\right) T_s(z) + W_s(z) = -2\mathrm{i}T\left(k^{(1)} \cdot \nabla_{1X}\right) A_1, \tag{C 7}$$

$$\left(\mathrm{D}^2 - k^2\right)^2 W_s(z) = -4\mathrm{i}\left(\mathrm{D}^2 W - k^2 W\right)\left(k^{(1)} \cdot \nabla_{1X}\right) A_1, \tag{C 8}$$

and the boundary condition at $z = 1$

$$\mathrm{D}^2 W_s + k^2 Ma_c T_s = -k^2 Ma^{(1)} T A_1 + 2\mathrm{i}Ma_c T\left(k^{(1)} \cdot \nabla_{1X}\right) A_1. \tag{C 9}$$

REFERENCES

ASSENHEIMER, M. & STEINBERG, V. 1996 Observation of coexisting upflow and downflow hexagons in Boussinesq Rayleigh–Bénard convection. *Phys. Rev. Lett.* **76**, 756–760.

BÉNARD, H. 1900 Les tourbillons cellulaires dans une nappe liquide. *Rev. Gén. Sci. Pures Appl.* **11**, 1261–1271.

BLOCK, M. J. 1956 Surface tension as the cause of Bénard cells and surface deformation in a liquid film. *Nature* **178**, 650–651.

BRAGARD, J. & LEBON, G. 1993 Non-linear Marangoni convection in a layer of finite depth. *Europhys. Lett.* **21**, 831–836.

BRAND, H. R. 1989 Envelope equations near the onset of a hexagonal pattern. *Prog. Theor. Phys. Suppl.* **99**, 442–449.

BUSSE, F. H. 1967 The stability of finite ampitude cellular convection and its relation to an extremum principle. *J. Fluid Mech.* **30**, 625–649.

BUSSE, F. H. 1978 Non-linear properties of thermal convection. *Rep. Prog. Phys.* **41**, 1929–1967.

CAROLI, B., CAROLI, C. & ROULET, B. 1984 On the stability of hexagonal interfacial patterns in directional solidification of binary mixtures. *J. Cryst. Growth* **68**, 677–690.

CASTILLO, J. L. & VELARDE, M. G. 1982 Buoyancy-thermocapillary instability: the role of interfacial deformation in one- and two-component fluid layers heated from below or above. *J. Fluid. Mech.* **125**, 463–474.

CERISIER, P., JAMOND, C., PANTALONI, J. & PÉREZ-GARCIA, C. 1987 Stability of roll and hexagonal patterns in Bénard-Marangoni convection. *Phys. Fluids* **30**, 954–959.

CHRISTOV, C. I., PONTES, J. & VELARDE, M. G. 1996 Splitting methods for free-surface viscous fluids subject to thermal Marangoni effects. In *Advanced Concepts and Techniques in Thermal Modeling* (ed. D. Lemonier, J. B. Saulnier & M. Fiebig), pp. 142–148. Elsevier.

CLOOT, A. & LEBON, G. 1984 A non-linear stability analysis of the Bénard-Marangoni problem. *J. Fluid Mech.* **145**, 447–469.

CROSS, M. C. & HOHENBERG, P. C. 1993 Pattern formation outside of equilibrium. *Rev. Mod. Phys.* **65**, 851–1112.

DAUBY, P. C. & LEBON, G. 1996 Bénard-Marangoni instability in rigid rectangular containers. *J. Fluid Mech.* **329**, 25–64.

DAVIS, S. H. 1969 Buoyancy-surface tension instability by the method of energy. *J. Fluid. Mech.* **39**, 347–359.

DAVIS, S. H. 1987 Thermocapillary instabilities. *Ann. Rev. Fluid Mech.* **19**, 403–435.

DAVIS, S. H. & HOMSY, G. M. 1980 Energy stability theory for free-surface problems: buoyancy-thermocapillary layers. *J. Fluid. Mech.* **98**, 527–538.

DRAZIN, P. G. & REID, W. H. 1981 *Hydrodynamic Stability*. Cambridge University Press.

EDWARDS, W. S. & FAUVE, S. 1993 Parametrically excited quasicrystalline surface waves. *Phys. Rev. E* **47**, 788–801.

GOLOVIN, A. A., NEPOMNYASHCHY, A. A., & PISMEN, L. M. 1995 Pattern formation in large-scale Marangoni convection with deformable interface. *Physica D* **81**, 117–147.

GOLUBITSKY, M., SWIFT, J. W. & KNOBLOCH, E. 1984 Symmetries and pattern selection in Rayleigh-Bénard convection. *Physica D* **10**, 249–276.

GUNARATNE, G. H. 1993 Complex spatial patterns on plannar continua. *Phys. Rev. Lett.* **71**, 1367–1370.

HADJI, L. 1996 Nonlinear analysis of the coupling between interface deflection and hexagonal patterns in Rayleigh-Bénard-Marangoni convection. *Phys. Rev. E* **53**, 5982–5992.

HOYLE, R. B. 1995 Nonlinear phase diffusion equations for the long-wave instabilities of hexagons. *Appl. Math. Lett.* **8**, 81–85.

KNOBLOCH, E. 1990 Pattern selection in long-wavelength convection. *Physica D* **41**, 450–479.

KOSCHMIEDER, E. L. 1993 *Bénard Cells and Taylor Vortices*. Cambridge University Press.

KOSCHMIEDER, E. L. & PRAHL, S. 1990 Surface tension driven Bénard convection in small containers. *J. Fluid Mech.* **215**, 571–593.

KUBSTRUP, C., HERRERO, H. & PÉREZ-GARCÍA, C. 1996 Fronts between hexagons and squares in a generalized Swift-Hohenberg equation. *Phys. Rev. E* **54**, 1560–1569.

MALKUS, W. V. R. & VERONIS, G. 1958 Finite amplitude cellular convection. *J. Fluid Mech.* **4**, 225–260.

MALOMED, B. A., NEPOMNYASHCHY, A. A. & TRIBELSKY, M. I. 1989 Two-dimensional quasiperiodic structures in nonequilibrium systems. *Sov. Phys. JETP* **69**, 388–397.

MANNEVILLE, P. 1990 *Dissipative Structures and Weak Turbulence*. Academic.

NEWELL, A. C. & WHITEHEAD, J. A. 1969 Finite bandwidth, finite amplitude convection. *J. Fluid Mech.* **38**, 279–303.

NITSCHKE, K. & THESS, A. 1995 Secondary instability in surface tension driven Bénard convection. *Phys. Rev. E* **52**, 5772–5775.

NORMAND, C., POMEAU, Y. & VELARDE, M. G. 1977 Convective instability: A physicist's approach. *Rev. Mod. Phys.* **49**, 581–624.

OSTRACH, S. 1982 Low-gravity fluid flows. *Ann. Rev. Fluid Mech.* **14**, 313–345.

PAMPALONI, E., PÉREZ-GARCÍA, C., ALBAVETTI, L. & CILIBERTO, S. 1992 Transition from hexagons to rolls in convection in fluids under non-Boussinesq conditions. *J. Fluid Mech.* **234**, 393–416.

PEARSON, J. R. A. 1958 On convection cells induced by surface tension. *J. Fluid Mech.* **4**, 489–500.

RAYLEIGH, LORD 1916 On convection currents in a horizontal layer of fluid, when the higher temperature is on the under side. *Phil. Mag.* **32**, 529–538.

SCANLON, J. W. & SEGEL, L. A. 1967 Finite amplitude cellular convection induced by surface tension. *J. Fluid Mech.* **30**, 149–162.

SCHATZ, M. F., VANHOOK, S. J., MCCORMICK, W. D., SWIFT, J. B. & SWINNEY, H. L. 1995 Onset of surface-tension-driven Bénard convection. *Phys. Rev. Lett.* **75**, 1938–1941.

SCHLÜTER, A., LORTZ, D. & BUSSE, F. H. 1965 On the stability of steady finite amplitude convection. *J. Fluid Mech.* **23**, 129–144.

SEGEL, L. A. 1965 The non-linear interaction of a finite number of disturbances to a layer of fluid heated from below. *J. Fluid Mech.* **21**, 359–384.

SEGEL, L. A. 1969 Distant sidewalls cause slow amplitude modulation of cellular convection. *J. Fluid Mech.* **38**, 203–224.

SEGEL, L. A. & STUART, J. T. 1962 On the question of the preferred mode in cellular thermal convection. *J. Fluid Mech.* **13**, 289–306.

SHTILMAN, L. & SIVASHINSKY, G. I. 1991 Hexagonal structure of large-scale Marangoni convection. *Physica* D **52**, 477–488.

SIVASHINSKY, G. I. 1982 Large cells in nonlinear Marangoni convection. *Physica* D **4**, 227–235.

SUSHCHIK, M. M. & TSIMRING, L. S. 1994 The Eckhaus instability in hexagonal patterns. *Physica* D **74**, 90–106.

THESS, A. & BESTEHORN, M. 1995 Planform selection in Bénard-Marangoni convection: l-h̃exagons versus g-h̃exagons. *Phys. Rev. E* **52**, 6358–6367.

THESS, A. & ORSZAG, S. A. 1995 Surface-tension-driven Bénard convection at infinite Prandtl number. *J. Fluid Mech.* **283**, 201–230.

VANHOOK, S. J., SCHATZ, M. F., MCCORMICK, W. D., SWIFT, J. B. & SWINNEY, H. L. 1995 Long-wavelength instability in surface-tension-driven Bénard convection. *Phys. Rev. Lett.* **73**, 932–936.

VELARDE, M. G. & CASTILLO, J. L. 1982 Transport and reactive phenomena leading to interfacial instability. In *Convective transport and instability phenomena* (ed. J. Zierep & H. Oertel), pp. 235–264, Braun-Verlag, Karlsruhe.

VELARDE, M. G. & NORMAND, C. 1980 Convection. *Sci. Am.* **243**, 92–108.

VIDAL, A. & ACRIVOS, A. 1966 Nature of the neutral state in surface-tension driven convection. *Phys. Fluids* **9**, 615–616.

WOLFRAM, S. 1993 *Mathematica*. Addison-Wesley.